J. Fluid Mech. (2024), *vol.* 990, A11, doi:10.1017/jfm.2024.512

JFM PAPERS

Dynamics of weighted flexible ribbons in a uniform flow

Kui Liu[1] **and Haibo Huang**[1],†

[1]Department of Modern Mechanics, University of Science and Technology of China, Hefei, Anhui 230026, PR China

(Received 16 December 2023; revised 14 April 2024; accepted 14 May 2024)

This study explores the dynamics of flexible ribbons with an added weight G at the tail in uniform flow, considering key parameters like inflow Reynolds number (Re_u), mass ratio (M_t) and aspect ratio ($\mathcal{R}$). For two-dimensional ribbons, a simplified theoretical model accurately predicts equilibrium configurations and forces. Inspired by Barois & De Langre (*J. Fluid Mech.*, vol. 735, 2013, R2), we introduce an important control parameter (C_G) that effectively collapses normalized forces and angle data. Vortex-induced vibration is observed, and Strouhal number (St) scaling laws with C_G are identified. In three-dimensional scenarios, the model effectively predicts lift, but its accuracy in predicting drag is limited to situations with small Re_u values. The flow along the side edges mitigates pressure differences, thereby suppressing vibration and uplift, particularly noticeable in the case of narrow ribbons. This study offers new insights into the dynamics of flexible bodies in uniform flow.

Key words: flow-structure interactions, drag reduction

1. Introduction

The interaction between flexible structures and surrounding fluids is a common and well-known phenomenon in nature, as seen in the reconfiguration of plants (de Langre 2008), flapping of flags (Shelley & Zhang 2011), swimming fish (Triantafyllou, Triantafyllou & Yue 2000) and the flight of birds/insects (Wu 2011). Studying the dynamics of these fluid–flexible structure systems is valuable for biologists seeking a deeper understanding of plant biology and the locomotion of aquatic and aerial animals (Nepf 2012; Lauder 2015). Moreover, the fundamental mechanisms uncovered can serve as inspiration for engineers designing high-performance biomimetic aerial/underwater vehicles or robots (Platzer *et al.* 2008; Smits 2019). The applications extend to energy extraction (Allen & Smits 2001; Wu 2011; Mathai *et al.* 2022), the paper industry (Watanabe *et al.* 2002) and flow control (Shen *et al.* 2003; Sunil, Kumar & Poddar 2022). As a result, these issues have captivated human interest for several decades.

† Email address for correspondence: huanghb@ustc.edu.cn

Previous studies, such as Alben, Shelley & Zhang (2002), Gao *et al.* (2020) and Sun *et al.* (2022), have focused on drag reduction in fluid–flexible structure interactions. Classic theory for rigid bluff bodies suggests that drag (F_d) is proportional to the square of the oncoming flow speed (U), i.e. $F_d \sim U^2$ (Batchelor 1967). However, flexible bodies under fluid loading undergo reconfiguration, decreasing the projected area perpendicular to the flow and adopting a more streamlined posture (Alben *et al.* 2002; Buchak, Eloy & Reis 2010; Luhar & Nepf 2011; Schouveiler & Eloy 2013). This reconfiguration results in a slower-growing form of drag, expressed as $F_d \sim U^{2+\mathscr{V}}$, where $\mathscr{V}$ is the Vogel exponent (Vogel 1984, 1989). Examples like tree leaves (Vogel 1989) or circular plastic sheets (Schouveiler & Boudaoud 2006) demonstrate a much slower drag growth than the U^2 law as they roll into tighter cones in the fluid. In a two-dimensional (2-D) flowing soap film, a flexible fibre tethered at the midpoint exhibits drag scaling as $U^{4/3}$ (i.e. $\mathscr{V} = -2/3$) at high Reynolds numbers (*Re*), as observed in the experimental and theoretical study by Alben *et al.* (2002) and Alben, Shelley & Zhang (2004). Additionally, Zhu (2008) numerically studied a compliant fibre tethered in a viscous flow at moderate *Re* (i.e. $Re \in [10, 800]$) and found that the power law exponents decrease monotonically from approximately 2 towards 4/3 as *Re* increases. Experimental investigations by Barois & de Langre (2013) on the reconfiguration of flexible ribbons with added weight at the free end revealed that drag is nearly independent of free-stream velocity at high *Re*. This unique phenomenon is a focal point of the present study. In nature, plants laden with fruits naturally droop and sway in the wind. Similarly, in everyday scenarios, heavy objects are often added to the trailing edge of flags to prevent violent flapping. These observations highlight the relevance of weighted flexible structures in both natural and engineered systems.

However, the aforementioned studies do not address the flapping or vibration of bodies. When flow passes a bluff body, vortex shedding typically occurs with significant flow separation at relatively high *Re*. In such cases, a vortex wake, such as the Kármán vortex street, becomes observable. The periodic shedding of vortices results in oscillatory forces acting on the body, causing drag and lift in the streamwise and transverse directions, respectively. If the body is elastically mounted, it may undergo substantial vibration, termed vortex-induced vibration (VIV) (Williamson & Govardhan 2004). There is an extensive body of literature on VIV of rigid objects, including works by Sarpkaya (2004), Wu, Ge & Hong (2012), Raissi *et al.* (2019), Carlson, Currier & Modarres-Sadeghi (2021) and Han *et al.* (2023), for interested readers to explore.

In the presence of an oncoming flow, flexible structures like flags, fibres or filaments may exhibit passive flapping motions (Zhang *et al.* 2000; Jia *et al.* 2007; Jia & Yin 2008; Kim *et al.* 2013). Taneda (1968) experimentally explored various flags and observed that flags remain motionless in slow flows, transitioning to regular and irregular flapping states as the flow speed increases. The motion of flexible filaments in a flowing soap film was investigated by Zhang *et al.* (2000), revealing two distinct dynamical states for a single filament: stretched–straight and coherent flapping states. Shelley, Vandenberghe & Zhang (2005) studied oscillations of heavy flags through experiments and theoretical analysis, identifying a critical flow velocity triggering flag flapping. The corresponding Strouhal number (*St*) is consistent with that of swimming/flying animals for efficient cruising (Taylor, Nudds & Thomas 2003). Eloy *et al.* (2008) conducted experiments on the flutter of flexible plates with varying aspect ratios, highlighting the significance of three-dimensional (3-D) effects. Numerous numerical studies complement these experiments. For instance, 2-D simulations of a flag in viscous flow by Zhu & Peskin (2002) and Connell & Yue (2007), or inviscid flow by Alben & Shelley (2008) confirmed bistable properties or hysteresis observed in experiments by Zhang *et al.* (2000) and

Shelley *et al.* (2005). Connell & Yue (2007), by altering the mass ratio of 2-D flags and fluid, identified three distinct regimes: fixed-point, regular flapping and chaotic flapping regimes. The flapping of 3-D flags was simulated by Kim & Peskin (2007) and Huang & Sung (2010), considering the effects of gravity. Additional numerical simulations of flexible flags or filaments can be found in works by Zhu & Peskin (2003), Zhu (2009), Uddin, Huang & Sung (2013), O'Connor & Revell (2019) and others.

In this study, we numerically investigate the dynamics of flexible ribbons in a uniform flow, with a weight G added at the trailing edges. Notably, the only existing experimental research on this specific fluid–flexible structure problem was conducted by Barois & de Langre (2013). However, their study lacked comprehensive discussion, omitting crucial details such as flow fields, potentially due to experimental measurement challenges. Additionally, they did not account for the effects of aspect ratio ($\mathcal{R}$) and the 2-D cases, which could yield notably different results, particularly when vibrations occur with a large aspect ratio. Furthermore, their study neglected viscous effects given the sufficiently large *Re*. To address these limitations, we conduct both 2-D and 3-D simulations at low Reynolds numbers ($\sim O(10^2)$). Our investigation involves a thorough examination of ribbon reconfiguration and forces, and we establish a simplified theoretical model based on force decomposition for accurate predictions. Force decomposition allows us to isolate tangential forces, enabling a closer examination of viscous effects. Special attention is given to ribbon vibrations and the derivation of scaling laws. Additionally, we explore 3-D effects by varying the aspect ratio, conducting a detailed analysis of both 2-D and 3-D flow fields.

Adding weight to the end of the flexible ribbon serves several purposes in our study. Firstly, it simulates gravity's effect on flexible structures encountered in real-world scenarios. Our goal is to understand how gravity influences their motion and deformation. Secondly, adding weight enables us to manipulate the system's dynamic behaviour. Adjusting the centre of mass affects dynamic characteristics like vibration frequency, amplitude and mode shape of the ribbon. This provides more control variables and experimental parameters, enhancing our understanding of fluid–structure interaction. Furthermore, this approach offers insights and strategies for designing and optimizing flexible structures. Optimizing weight distribution improves performance across aerospace and mechanical engineering. For example, in flexible unmanned aerial vehicles, added weights may enhance flight dynamics.

Note that both 2-D and 3-D simulations are essential in our study. Considering that achieving a much wider range of $\mathcal{R}$ would demand significant computational resources, we selected a feasible range that still allowed us to investigate relevant 3-D effects. The 2-D simulations are valuable as they correspond to cases where $\mathcal{R}$ approaches infinity, assuming deformation in the spanwise direction can be neglected. This simplification enables us to focus on the fundamental behaviour of the ribbon and its interaction with the surrounding fluid. Besides, conducting 2-D simulations aligns with our theoretical analysis, which is inherently two-dimensional. This allows for a direct comparison between theoretical predictions and numerical simulations, facilitating a deeper understanding of the fluid–structure interaction phenomenon.

The remainder of this paper is organized as follows. In § 2, we present the physical problem and mathematical formulation. The numerical method and validation are detailed in § 3. In § 4, we discuss comprehensive results, and concluding remarks are provided in § 5.

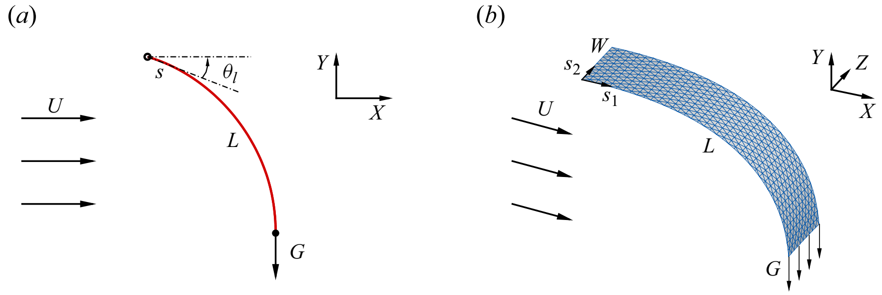

Figure 1. Schematic diagrams illustrating 2-D (*a*) and 3-D (*b*) flexible ribbons in a uniform flow. Here, U represents the oncoming flow speed, L and W denote the chord and span length of the ribbon, respectively, G is the weight added at the trailing edge, θ_l is the angle between the tangent direction of the leading edge and the horizontal direction and s as well as (s_1, s_2) represent the curvilinear coordinates on the ribbons.

2. Physical problem and mathematical formulation

The schematic diagrams of the 2-D and 3-D flexible ribbons considered in our study are illustrated in figure 1. These flexible ribbons, characterized by a length L (and width W in 3-D cases), are immersed in a uniform flow with an oncoming speed U. The leading edge of the ribbon is stationary, while a weight G is affixed at the trailing edge, inducing a natural droop. The remaining sections of the ribbon have the freedom to move and passively deform, facilitated by fluid–structure interactions.

We employ the incompressible Navier–Stokes equations to model and solve the fluid flow,

$$\frac{\partial \boldsymbol{v}}{\partial t} + \boldsymbol{v} \boldsymbol{\cdot} \boldsymbol{\nabla} \boldsymbol{v} = -\frac{1}{\rho}\boldsymbol{\nabla} p + \frac{\mu}{\rho}\nabla^2 \boldsymbol{v} + \boldsymbol{f}_b, \tag{2.1}$$

$$\boldsymbol{\nabla} \boldsymbol{\cdot} \boldsymbol{v} = 0, \tag{2.2}$$

where $\boldsymbol{v}$ is the velocity, p is the pressure, ρ is the density of the fluid, μ is the dynamic viscosity and $\boldsymbol{f}_b$ denotes the Eulerian momentum force acting on the surrounding fluid due to the immersed boundary.

To characterize the deformation and motion of the ribbon within a Lagrangian coordinate system, we employ the structural equation. In the case of 3-D scenarios, the structural equation is formulated as follows (Huang & Sung 2010; Hua, Zhu & Lu 2014):

$$\rho_s h \frac{\partial^2 \boldsymbol{X}}{\partial t^2} = \sum_{i,j=1}^{2} \frac{\partial}{\partial s_i}\left\{\varphi_{ij}\left[\delta_{ij} - \left(\frac{\partial \boldsymbol{X}}{\partial s_i} \boldsymbol{\cdot} \frac{\partial \boldsymbol{X}}{\partial s_j}\right)^{-1/2}\right]\frac{\partial \boldsymbol{X}}{\partial s_j} - \frac{\partial}{\partial s_j}\left(\gamma_{ij}\frac{\partial^2 \boldsymbol{X}}{\partial s_i \partial s_j}\right)\right\} + \boldsymbol{F}_s + \boldsymbol{F}_g, \tag{2.3}$$

where $\boldsymbol{X}(s_1, s_2, t) = (X(s_1, s_2, t), Y(s_1, s_2, t), Z(s_1, s_2, t))$ is the position vector of the ribbon, s_1 and s_2 are the chordwise and spanwise Lagrangian coordinates, respectively, ρ_s is the structural mass density, h is the structural thickness, $\boldsymbol{F}_s$ is the Lagrangian force exerted on the plate by the surrounding fluid, $\boldsymbol{F}_g = G\boldsymbol{g}/g$ is the weight added at the trailing edge (here, g is the magnitude of gravitational acceleration $\boldsymbol{g}$) and δ_{ij} is the Kronecker delta function. Matrix φ_{ij} is the in-plane effect matrix, where $\varphi_{11} = \varphi_{22} = Eh$ is the structural stretching stiffness and φ_{12} is the structural shearing stiffness. Matrix γ_{ij} represents the out-of-plane effect matrix associated with bending and twisting stiffness, where $\gamma_{11} = EI$ denotes the chordwise bending stiffness. At the leading edge ($s_1 = 0$), the simply supported condition is adopted, i.e.

$$\boldsymbol{X} = (0, 0, s_2), \quad \frac{\partial^2 \boldsymbol{X}}{\partial s_1^2} = 0. \tag{2.4a,b}$$

At the trailing edge ($s_1 = L$) and two other free edges ($s_2 = 0$ or W), the boundary conditions are

$$\varphi_{ij} \left[\delta_{ij} - \left(\frac{\partial \boldsymbol{X}}{\partial s_i} \cdot \frac{\partial \boldsymbol{X}}{\partial s_j} \right)^{-1/2} \right] \frac{\partial \boldsymbol{X}}{\partial s_j} - \frac{\partial}{\partial s_j} \left(\gamma_{ij} \frac{\partial^2 \boldsymbol{X}}{\partial s_i \partial s_j} \right) = 0, \quad \frac{\partial^2 \boldsymbol{X}}{\partial s_i \partial s_j} = 0. \tag{2.5a,b}$$

Here, the Einstein summation convention is not applied on i and j ($i, j = 1, 2$). In addition, the weight $G = W m_t g$ is evenly distributed at the trailing edge (see figure 1*b*), where m_t is the mass per unit length of the additional weight.

For the 2-D cases, the structural equation (2.3) degenerates into the following form (Zhu & Peskin 2002; Connell & Yue 2007; Hua, Zhu & Lu 2013):

$$\rho_s h \frac{\partial^2 \boldsymbol{X}}{\partial t^2} - \frac{\partial}{\partial s} \left[Eh \left(1 - \left| \frac{\partial \boldsymbol{X}}{\partial s} \right|^{-1} \right) \frac{\partial \boldsymbol{X}}{\partial s} \right] + EI \frac{\partial^4 \boldsymbol{X}}{\partial s^4} = \boldsymbol{F}_s + \boldsymbol{F}_g, \tag{2.6}$$

where s is the Lagrangian coordinate, $\boldsymbol{X}(s, t) = (X(s, t), Y(s, t))$ is the position vector of the ribbon. At the leading edge of the ribbon ($s = 0$), the simply supported condition (2.4*a*,*b*) becomes

$$\boldsymbol{X} = (0, 0), \quad \frac{\partial^2 \boldsymbol{X}}{\partial s^2} = 0. \tag{2.7a,b}$$

At the free end ($s = L$), the boundary conditions are

$$-Eh \left(1 - \left| \frac{\partial \boldsymbol{X}}{\partial s} \right|^{-1} \right) \frac{\partial \boldsymbol{X}}{\partial s} + EI \frac{\partial^3 \boldsymbol{X}}{\partial s^3} = 0, \quad \frac{\partial^2 \boldsymbol{X}}{\partial s^2} = 0. \tag{2.8a,b}$$

Besides, the weight $G = 1 \cdot m_t g$ (considering unit depth) is concentrated at the trailing edge (see figure 1*a*).

In our study, the fluid density ρ, the dynamic viscosity μ and the dimensional length of the ribbon L are fixed. To normalize the above equations, the characteristic quantities ρ, L and $U_{ref} = \kappa\mu/\rho L$ are chosen, where $\kappa = 200$ is a constant (note that other values of κ are also acceptable, and would not alter the trends and findings presented in our study). Therefore, the characteristic time is $T = L/U_{ref}$, and the gravitational acceleration is $g = U_{ref}^2/L$. Based on dimensional analysis, the following dimensionless governing parameters are introduced: the aspect ratio $\mathcal{R} = W/L$, the Reynolds number based on the oncoming flow speed $Re_u = \rho UL/\mu$, the mass ratio of the ribbon to the fluid $M = \rho_s h/\rho L$, the mass ratio of additional weight at the trailing edge to the fluid $M_t = m_t/\rho L^2$, the stretching stiffness $S = Eh/\rho U_{ref}^2 L$ and the bending stiffness $K = EI/\rho U_{ref}^2 L^3$.

3. Numerical method and validation

The lattice Boltzmann method (Chen & Doolen 1998) is employed for the numerical solution of the Navier–Stokes equations, while a finite element method is utilized to model the motion of the flexible plate (Doyle 2001). The immersed boundary method (Zhu & Peskin 2002) is employed to couple the fluid and structure solvers. To enforce the no-slip

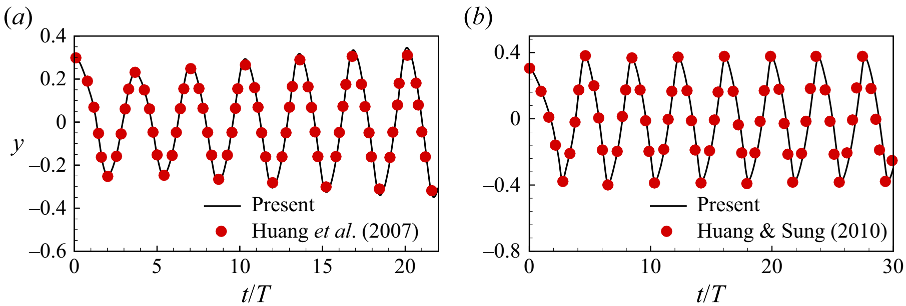

Figure 2. Validations for cases: (*a*) transverse displacement of the trailing edge of the 2-D flag with $Re = 200$, $K = 0.0015$, $M = 1.5$, $S = 1000$ and $Fr = 0.5$ (Huang, Shin & Sung 2007); (*b*) transverse displacement of the centre of the trailing edge of the 3-D flag with $Re = 200$, $K = 0.0001$, $M = 1.0$, $S = 1000$, $Fr = 0$ and $\AE = 1$ (Huang & Sung 2010).

boundary condition, the body force term $\boldsymbol{f}_b$ in (2.1) acts as an interaction force between the fluid and the immersed boundary. The deformation of the plate is addressed using the corotational scheme (Doyle 2001), which is adept at handling large displacements. Further details on the numerical methods can be found in our previous papers (Hua *et al.* 2013; Huang, Wei & Lu 2018; Zhang, Huang & Lu 2020).

The simulations are performed on a computational domain in the range $[-15, 25] \times [-15, 15]$ in the x and y directions for 2-D cases, and $[-10, 30] \times [-10, 10] \times [-10, 10]$ in the x, y and z directions for 3-D cases. This domain size is sufficiently large to eliminate any boundary effects. Initially, the fluid's velocity field is $U\boldsymbol{e}_x$ throughout the domain, where $\boldsymbol{e}_x$ is the unit vector in the x direction. A uniform velocity $U\boldsymbol{e}_x$ is imposed at the upstream boundary and the side boundaries of the fluid computational domain. At the downstream boundary, a convective boundary condition $\partial \boldsymbol{v}/\partial t + U\partial \boldsymbol{v}/\partial x = \boldsymbol{0}$ is specified.

To validate the numerical method, simulations of 2-D and 3-D flags in a uniform flow are conducted. In the 2-D case, the non-dimensional parameters are $Re = 200$, $K = 0.0015$, $M = 1.5$, $S = 1000$ and Froude number $Fr = gL/U^2 = 0.5$ (Huang *et al.* 2007). For the 3-D case, the parameters are $Re = 200$, $K = 0.0001$, $M = 1.0$, $S = 1000$, $Fr = 0$ and $\AE = 1$ (Huang & Sung 2010). The results are depicted in figure 2, showing good agreement with results in the literature (Huang *et al.* 2007; Huang & Sung 2010).

Besides, we have also made a direct comparison of our results with those of Barois & de Langre (2013), as shown in figure 3. In this comparison, the G-normalized drag F_d/G of the 3-D ribbon is presented as a function of C_G with $M_t = 1$ and $\AE = 0.5$, where the definition of C_G in 3-D scenarios is $C_G = \rho U^2 LW/2G$. Despite our Re_u being approximately one or two orders of magnitude smaller than theirs ($\sim O(10^2–10^3)$ compared with $\sim O(10^3–10^5)$), our results capture the variation trend of the F_d/G curve well. Especially when $C_G < 1$, our results are consistent with their experimental findings. This indicates the significance of our study within the $Re_u \sim O(10^2–10^3)$ range. However, for $C_G > 1$, we observe that our F_d/G values are notably larger than their corresponding values. This discrepancy may be due to the significant skin friction caused by viscous effects in our study, owing to our lower Re_u, as discussed in § 4.2.1.

Furthermore, our numerical strategy has been successfully validated and applied to study various flow problems, including tandem flexible inverted flags in a uniform flow (Huang *et al.* 2018), the impact of trailing-edge shape on the self-propulsive performance of heaving flexible plates (Zhang *et al.* 2020) and the scaling laws of the self-propulsive

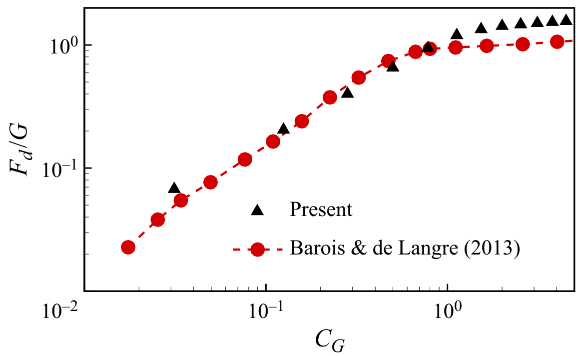

Figure 3. The G-normalized drag F_d/G of the 3-D ribbon as a function of C_G with $M_t = 1$ and $AR = 0.5$. The experimental results of Barois & de Langre (2013) are also presented with $AR \approx 0.1$.

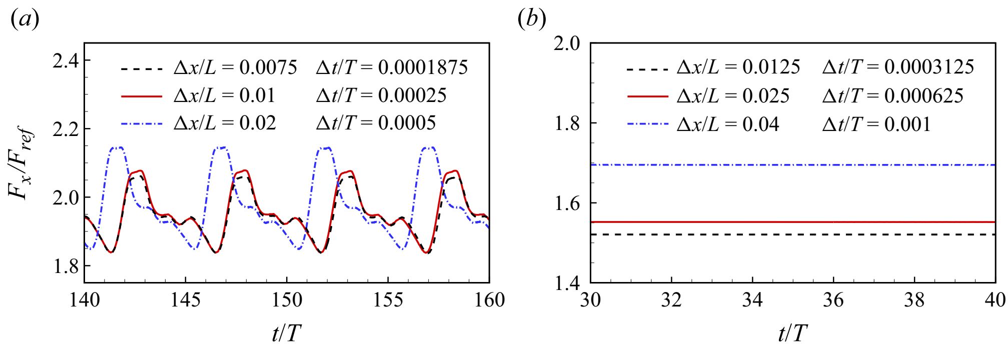

Figure 4. Grid independence and time-step independence study for (*a*) the 2-D ribbon with $M_t = 1$ and $Re_u = 200$ and (*b*) the 3-D ribbon with $M_t = 1$, $Re_u = 200$ and $AR = 0.25$. The streamwise force F_x normalized by $F_{ref} = (1/2)\rho U_{ref}^2 L$ as a function of time is presented.

performance of flexible plates (Liu, Liu & Huang 2022). Additional detailed numerical validations are available in these referenced papers.

The outcomes of the grid independence and time-step independence assessments for the 2-D and 3-D flexible ribbons are depicted in figure 4. It indicates that $\Delta x/L = 0.01$ and $\Delta t/T = 0.00025$ are suitable for the 2-D cases, while $\Delta x/L = 0.025$ and $\Delta t/T = 0.000625$ are sufficient for the 3-D cases to attain accurate results. Consequently, we adopt these mesh sizes and time-step sizes in our subsequent simulations.

4. Results and discussion

In the present simulations, certain parameters are held constant: mass ratio of the ribbon to the fluid ($M = 0.5$), bending stiffness ($K = 10^{-4}$) and stretching stiffness ($S = 10^4$). The choice of a large S ensures that the ribbon is nearly inextensible, while a small K ensures that the ribbon is fully compliant with the surrounding flow, aligning with the experimental findings of Barois & de Langre (2013). The selected value for M also conforms to previous studies on flexible bodies in a uniform flow (Huang & Sung 2010; Hua *et al.* 2014; Sun *et al.* 2022), where M ranges from 10^{-1} to 10^0. The remaining key parameters, namely the inflow Reynolds number Re_u, the mass ratio of the additional weight at the trailing edge

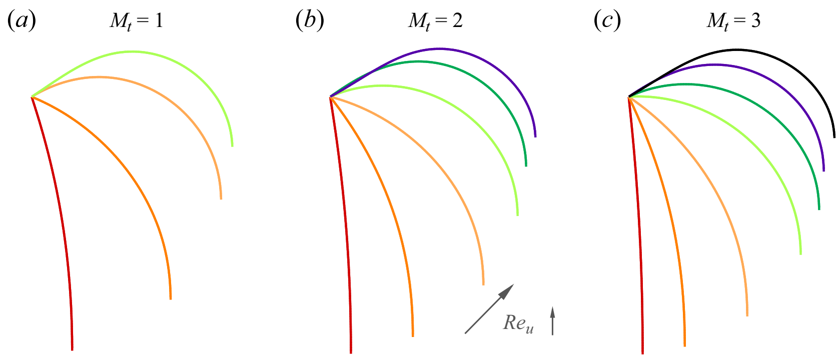

Figure 5. The equilibrium configurations of the ribbons for (*a*) $M_t = 1$, $Re_u = 100$–400, (*b*) $M_t = 2$, $Re_u = 100$–600 and (*c*) $M_t = 3$, $Re_u = 100$–700. Here, the curves represent time-averaged configurations, as the ribbons undergo periodic oscillation in 2-D scenarios. In each panel, the Re_u values of the cases increase gradually from left to right, with an interval of 100.

M_t and the aspect ratio $\mathcal{R}$, are left variable. Both 2-D and 3-D cases are considered, and the corresponding results are presented in §§ 4.1 and 4.2, respectively.

4.1. *Analysis of two-dimensional results*

In the 2-D scenarios, the aspect ratio $\mathcal{R} = \infty$, and we investigate the effects of Re_u ($\in [50, 800]$ with an interval of 50) and M_t ($= 1, 2$ and 3). In Appendix A, we demonstrate that the initial angle of the ribbon has no impact on the statistics of interest, such as time-averaged forces. Once released from the initial state, the system promptly reaches an equilibrium state, where the ribbon may undergo periodic oscillations.

Our initial focus is on quasi-static results (§ 4.1.1) to propose a simplified model (§ 4.1.2). In this context, quantitative results are presented as time-averaged values unless explicitly specified otherwise. For instance, the time-averaged drag and lift are defined as $F_d = f_1 \int_{t'}^{t'+1/f_1} F_x(t)\,\mathrm{d}t$ and $F_l = f_1 \int_{t'}^{t'+1/f_1} F_y(t)\,\mathrm{d}t$, respectively, where f_1 represents the dominant frequency or flapping frequency, and $F_x(t)$ and $F_y(t)$ denote the instantaneous streamwise and transverse forces of the ribbon. The analysis of kinematic characteristics (i.e. vibrations) and flow fields of the system will be conducted in § 4.1.4.

4.1.1. *Reconfiguration and forces*

The discussion on the reconfiguration of the ribbons is presented first, as depicted in figure 5. In slow flows (i.e. small Re_u), the ribbon sags downwards due to gravity acting on the trailing edge. As Re_u increases, the ribbon gradually lifts upwards with noticeable bending deformations (figure 5), presenting a more streamlined shape. The projection length of the ribbon in the x and y directions, denoted as L_x and L_y respectively, monotonically increases and decreases with the flow speed, as illustrated in figure 6. These observations align with the fundamental characteristics of flexible body reconfiguration in flow (Alben *et al.* 2002; Gosselin, de Langre & Machado-Almeida 2010).

It is noteworthy that higher speeds can induce self-collision of the ribbon due to violent vibrations (see § 4.1.4). This leads to simulation failure, and the corresponding cases are discarded. Thus, there exists a critical value of Re_u, denoted as Re_u^c, beyond which the system becomes unstable. The value of Re_u^c is dependent on the mass ratio of the weight added at the trailing edge M_t. We observed that, for $M_t = 1$, 2 and 3, the critical Reynolds

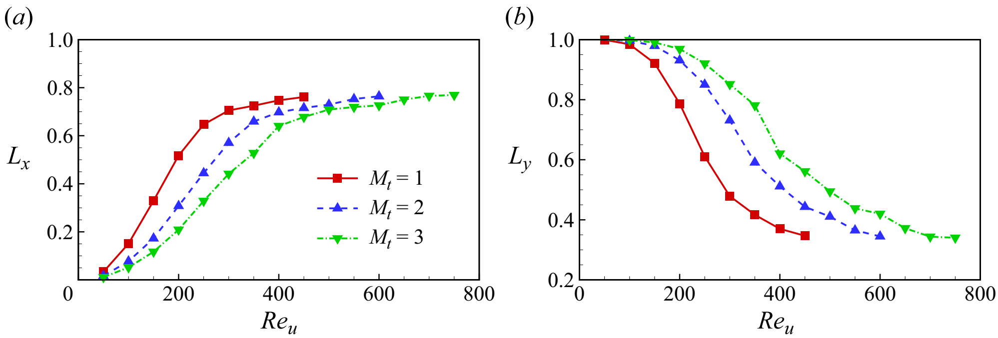

Figure 6. The normalized projected length of the ribbon in the x and y directions, i.e. (a) L_x and (b) L_y.

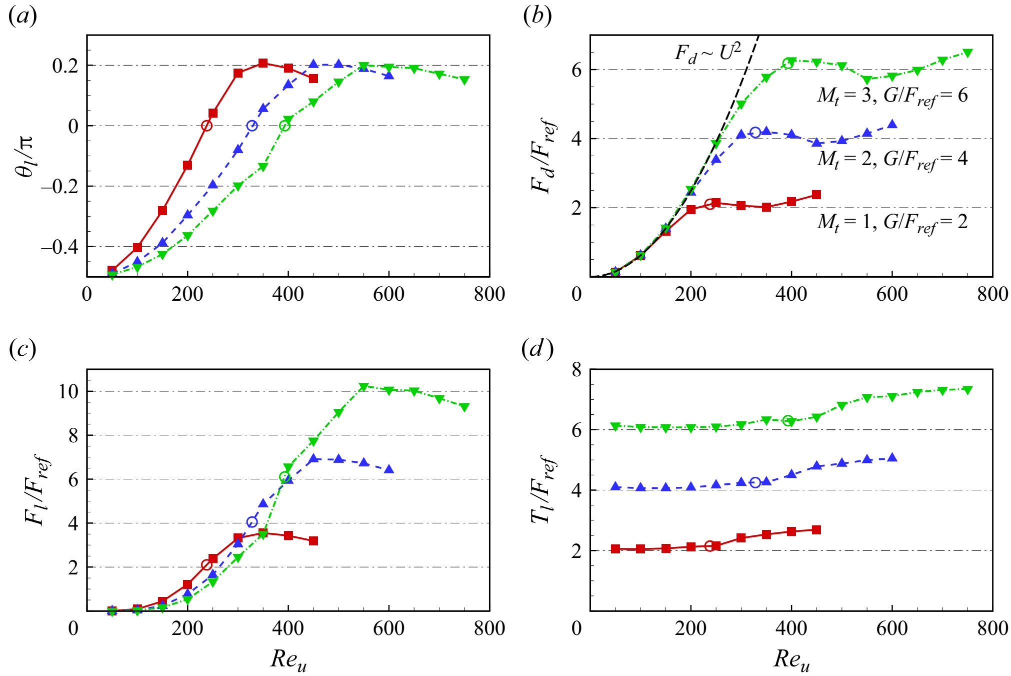

Figure 7. The normalized time-averaged (a) leading-edge inclination angle θ_l, (b) drag F_d, (c) lift F_l and (d) leading-edge tension T_l of the 2-D ribbons as functions of Re_u for various M_t. The hollow circles mark the positions where $\theta_l = 0$.

number Re_u^c is approximately 450, 600 and 750, respectively. Consequently, in figures 6 and 7, only cases with $Re_u \leq Re_u^c$ are plotted. This observation of Re_u^c increasing with M_t agrees with expectations, as a larger M_t typically enhances system stability.

In addition to L_x and L_y, the leading-edge inclination angle θ_l can also be employed to quantitatively describe the ribbon's reconfiguration (see figure 1a). Figure 7(a) illustrates θ_l as a function of Re_u. It is noted that θ_l exhibits an initial increase followed by a slight decrease with the increase of Re_u. The decrease in θ_l for large Re_u is associated with the increase in the streamwise projection length L_x of the ribbon (see figures 5 and 6(a), and note that the ribbon's total length remains constant due to its inextensibility). Its further mechanism will be discussed in figure 8. It is noteworthy that θ_l can significantly

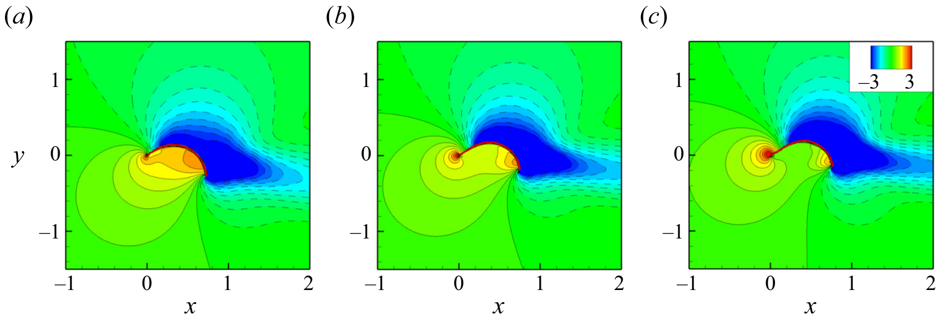

Figure 8. Time-averaged pressure contours around the ribbon for $Re_u = 350$ (*a*), 400 (*b*) and 450 (*c*) with $M_t = 1$. Solid and dashed lines denote the positive and negative normalized pressure contours, respectively.

exceed 0, as evident in figure 7(*a*), where the maximum value of θ_l is approximately 36°, or in figure 5, where the ribbon conspicuously protrudes upwards for large Re_u. This result diverges from the experiments conducted by Barois & de Langre (2013), where the maximum value of θ_l is 0. A more in-depth analysis of this disparity is provided in the subsequent sections.

The flow-induced reconfiguration significantly influences the forces acting on the ribbons (Schouveiler & Boudaoud 2006; Luhar & Nepf 2011). Figure 7(*b–d*) presents the time-averaged drag F_d, lift F_l and leading-edge tension T_l of the ribbon as functions of Re_u for different M_t. It is observed that, at small Re_u, the drag of the ribbon adheres well to the classical quadratic law, i.e. $F_d \sim Re_u^2 \sim U^2$ (see the dashed line in figure 7*b*). This behaviour is attributed to the minimal deformation of the ribbon at small Re_u. For instance, at $Re_u \leq 250$ with $M_t = 3$, the ribbon exhibits $L_y \geq 0.92$ (see figure 6*b*), resembling an upright rigid plate. Consequently, the drag of the ribbon at small Re_u mimics that of rigid bluff bodies. The U^2 growth in drag also implies the predominance of form drag while skin friction can be neglected (Alben *et al.* 2002). In the absence of skin friction, the tension of the ribbon is uniform and equivalent to the weight G added at the trailing edge (see § 4.1.2). Therefore, at small Re_u, the leading-edge tension T_l of the ribbon remains nearly constant (see figure 7*d*), i.e. $T_l \approx G$ (note that the value of normalized weight G/F_{ref} is twice that of M_t due to the factor 1/2 in $F_{ref} = (1/2)\rho U_{ref}^2 L$).

As Re_u increases, the influence of skin friction becomes significant. The hollow circles in figure 7 mark the positions where $\theta_l = 0$, signifying a point where skin friction starts to play a crucial role. Figure 7(*d*) indicates that, when $\theta_l > 0$, the leading-edge tension T_l experiences a substantial increase with the rising Re_u. This phenomenon may be attributed to the fact that, under large Re_u conditions ($\theta_l > 0$), the ribbon's shape tends to align more parallel to the oncoming flow (see figure 5), facilitating the generation of skin friction. Consequently, skin friction contributes to the tension in the ribbon, resulting in $T_l > G$ for high Re_u (figure 7*d*).

Here, we would like to estimate the magnitude of the skin friction to better elucidate whether it plays an important role. The skin friction can be approximated as viscous drag per unit width on a flat plate aligned with the flow, expressed as: $F_{vis} = 1.33\rho U^2 L_x Re_u^{-1/2}$ (Batchelor 1967; Alben *et al.* 2002) (i.e. the $U^{3/2}$ scaling), where L_x is the length of the plate (in our study, it is the projected length of the ribbon in the x direction). The dimensionless skin friction is given by: $\hat{F}_{vis} = F_{vis}/F_{ref} = 1.33\rho U^2 L_x Re_u^{-1/2}/(0.5\rho U_{ref}^2 L) = 2.66 Re_u^{3/2} L_x/(\kappa^2 L)$. Through calculation, when Re_u is small, F_{vis} is at least one order of magnitude smaller than the total drag F_d, indicating its negligible contribution (i.e. $F_{vis}/F_d < 10^{-1}$). Specifically, for the case with $Re_u = 400$ and $M_t = 2$, $F_{vis}/F_d \approx 0.09$, thus the skin friction can be ignored. However, at large Re_u, F_{vis} significantly increases. For instance, for $Re_u = 600$ and $M_t = 2$, $F_{vis}/F_d \approx 0.17$, which closely matches the percentage increase of T_l compared with G in figure 7(*d*). Alternatively, the approximate 17 % increase can be directly observed from figure 12(*a*). This indicates that, at large Re_u, the skin friction may have a significant effect on leading-edge tension increment. These conclusions are consistent with what we have found and summarized in the above analysis and § 4.1.2.

Remarkably, it is observed that, when $\theta_l > 0$, the change in F_d remains small, and F_d approximates G as Re_u increases (see figure 7*b*). In other words, the drag appears to be independent of the oncoming flow speed, resembling the findings of Barois & de Langre (2013). In the experiments by Barois & de Langre (2013), skin friction was neglected as $Re_u \sim O(10^4)$. Consequently, the tension in the ribbon equalled the weight added at the trailing edge, i.e. $T_l = G$. As Re_u increased, they observed that the leading edge of the ribbon remained horizontal (Barois & de Langre 2013), implying $\theta_l = 0$. Therefore, the drag remained constant since $F_d = T_l \cos\theta_l = G$ (see figure 25*a*). In contrast, in our study, θ_l continues to increase after reaching 0 (figure 7*a*), resulting in a further reduction in the transverse projection length L_y (figure 6*b*) and the form drag. However, the increased skin friction, as detailed in the next section, compensates for the reduced form drag, thereby maintaining the total drag substantially unchanged (figure 7*b*).

Concerning the lift F_l, it primarily relies on the transverse pressure difference across the ribbon. Notably, a larger transverse pressure difference results in a greater θ_l. Consequently, F_l exhibits a similar trend to θ_l as Re_u increases (see figure 7*c*). In figure 8, we present time-averaged pressure contours around the ribbon for $Re_u = 350$, 400 and 450 with $M_t = 1$. It is seen that, with the rise in Re_u, the high-pressure region beneath the ribbon diminishes and shifts towards the trailing edge, indicating a decrease in the pressure difference across the ribbon. Hence, beyond certain thresholds (e.g. $Re_u = 350$ for $M_t = 1$ and $Re_u = 450$ for $M_t = 2$), both F_l and θ_l decline as Re_u increases, as depicted in figure 7(*a*,*c*). Additionally, since $F_l = T_l \sin\theta_l + G$ (see figure 25*a*), it becomes evident that $F_l \approx G$ when $\theta_l = 0$ (indicated by the hollow circles in figure 7*c*).

Furthermore, it is observable that an increase in M_t (or the weight G) leads to an approximately proportional increase in T_l (figure 7*d*). This, in turn, results in a proportional increase in F_d and F_l when Re_u is large (figure 7*b*,*c*). Therefore, G emerges as a pivotal characteristic force of the system, offering insights for force rescaling in § 4.1.3.

4.1.2. *Simplified theoretical model*

To facilitate a more insightful analysis of the fluid–flexible structure problem, it is necessary to establish a simplified theoretical model. In Appendix B, we achieve this by decomposing the force acting on the ribbon. Next, we would like to check whether the model can effectively predict the equilibrium configurations and forces of the ribbons.

According to (B7), we can obtain the local inclination angle θ at different positions of the ribbon. Specifically, in (B7), let $\hat{s} = 0$ (i.e. the leading edge), we can get that

$$\theta_l = \theta(0) = -\frac{\pi}{2} + \frac{f_n L}{G}, \tag{4.1}$$

or

$$\frac{f_n L}{G} = \theta_l + \frac{\pi}{2}. \tag{4.2}$$

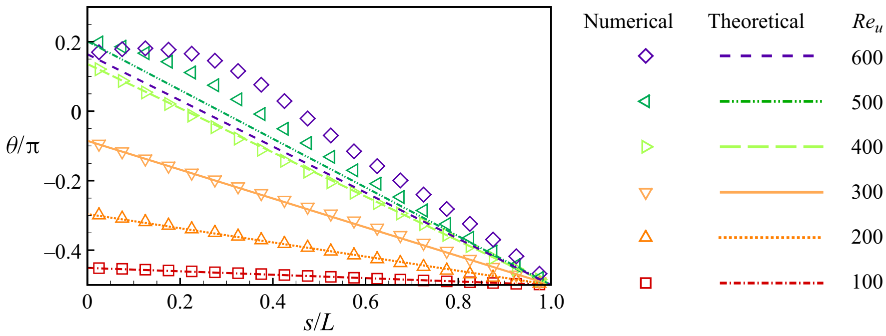

Figure 9. The local inclination angle θ along the ribbon for various Re_u with $M_t = 2$. Symbols and lines represent numerical and theoretical (according to (4.3)) results, respectively.

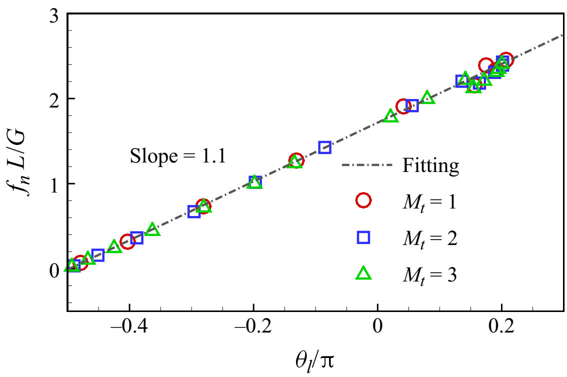

Figure 10. The G-normalized total normal force f_nL/G as a function of the leading-edge inclination angle θ_l for different M_t. The dash-dotted line is the fitting curve: $f_nL/G = \gamma(\theta_l + \pi/2)$, with a slope of $\gamma = 1.1$ and $R^2 = 0.99$.

Substituting (4.2) into (B7), we have

$$\theta(\hat{s}) = \theta_l - \hat{s}\left(\theta_l + \frac{\pi}{2}\right). \tag{4.3}$$

The equations (4.3) and (B7) describe the theoretical equilibrium shape of the ribbon. In practical terms, (4.3) is more useful than (B7) because it is more convenient to observe θ_l rather than f_n in experiments. Figure 9 shows the local inclination angle θ along the ribbon for various Re_u with $M_t = 2$, where symbols and lines represent numerical and theoretical (according to (4.3)) results, respectively. It is seen that the theoretical model effectively predicts θ along the ribbon when Re_u is not too large. However, the model fails for large Re_u, primarily because, under those circumstances, the large tangential force stretches the ribbon in the streamwise direction, and the shape is no longer a circular arc (see the cases with large Re_u in figure 5).

This theoretical model is also applicable for predicting the drag and lift of the ribbon. Although (4.2) has provided the relationship between f_n and θ_l, we aim to validate the results through numerical simulations. Figure 10 illustrates the G-normalized total normal force f_nL/G as a function of the leading-edge inclination angle θ_l. It is observed that, for all M_t, f_nL/G well satisfies the linear relationship with respect to θ_l with the slope $\gamma = 1.1$, while the slope given by (4.2) is 1. This slight difference may arise from the non-uniform

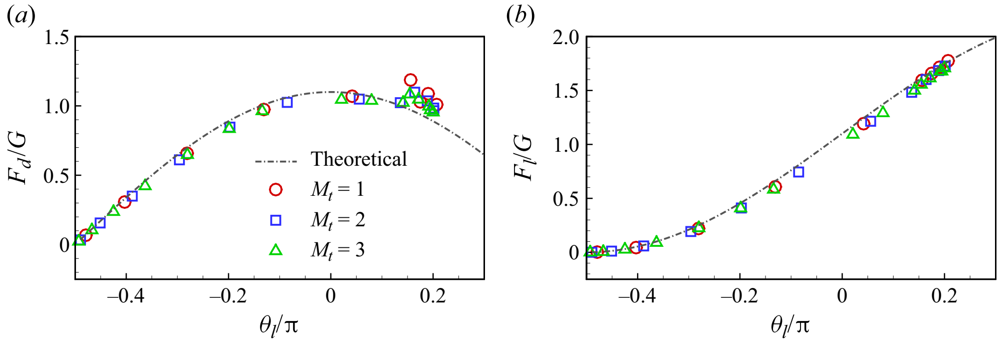

Figure 11. The G-normalized (a) drag F_d/G and (b) lift F_l/G as functions of θ_l for various M_t. The dash-dotted lines represent the theoretical predictions given by (4.5) and (4.6).

distribution of f_n near the edges (see figure 26a). The tangential force might also influence the slope as it alters the ribbon shape (i.e. θ_l) and local tension magnitude. Considering these factors, γ can be regarded as a correction parameter, and (4.2) can be modified to

$$f_n = \frac{\gamma G}{L}\left(\theta_l + \frac{\pi}{2}\right), \quad (\gamma = 1.1). \tag{4.4}$$

According to (4.3) and (4.4), the total drag F_d and lift F_l of the ribbon can be calculated as follows:

$$F_d = \int_0^1 -f_n \sin\theta \cdot L\,\mathrm{d}\hat{s} = \int_0^1 -\frac{\gamma G}{L}\left(\theta_l + \frac{\pi}{2}\right)\sin\left[\theta_l - \hat{s}\left(\theta_l + \frac{\pi}{2}\right)\right]\cdot L\,\mathrm{d}\hat{s}$$
$$= \gamma G \cos\theta_l, \tag{4.5}$$

$$F_l = \int_0^1 f_n \cos\theta \cdot L\,\mathrm{d}\hat{s} = \int_0^1 \frac{\gamma G}{L}\left(\theta_l + \frac{\pi}{2}\right)\cos\left[\theta_l - \hat{s}\left(\theta_l + \frac{\pi}{2}\right)\right]\cdot L\,\mathrm{d}\hat{s}$$
$$= \gamma G(1 + \sin\theta_l). \tag{4.6}$$

Figure 11 presents the G-normalized drag F_d/G and lift F_l/G. The numerical results align well with the theoretical values given by (4.5) and (4.6). However, small discrepancies are noticed for cases with $\theta_l \approx 0.2\pi$ (see figure 11a). This is not surprising as the assumptions made in the theoretical prediction, $f_n \approx C$ and $f_\tau \approx 0$, are broken in these large-Re_u cases.

Next, we examine the contribution of normal and tangential forces to drag and lift (i.e. the x and y component forces experienced by the ribbon). Let us begin by investigating the contribution of normal and tangential forces to drag

$$F_{n,x} = f_1 \int_{t'}^{t'+1/f_1} \int_0^L f_{n,x}(s,t)\,\mathrm{d}s\,\mathrm{d}t, \quad F_{\tau,x} = f_1 \int_{t'}^{t'+1/f_1} \int_0^L f_{\tau,x}(s,t)\,\mathrm{d}s\,\mathrm{d}t, \tag{4.7a,b}$$

where f_1 is the vibration frequency of the ribbon (see § 4.1.4). The contribution of normal and tangential forces to lift

$$F_{n,y} = f_1 \int_{t'}^{t'+1/f_1} \int_0^L f_{n,y}(s,t)\,\mathrm{d}s\,\mathrm{d}t, \quad F_{\tau,y} = f_1 \int_{t'}^{t'+1/f_1} \int_0^L f_{\tau,y}(s,t)\,\mathrm{d}s\,\mathrm{d}t. \tag{4.8a,b}$$

In figure 12, we present these forces as functions of Re_u for cases with $M_t = 2$. It is observed that, when $Re_u \leq 300$, the drag almost entirely comes from the normal force

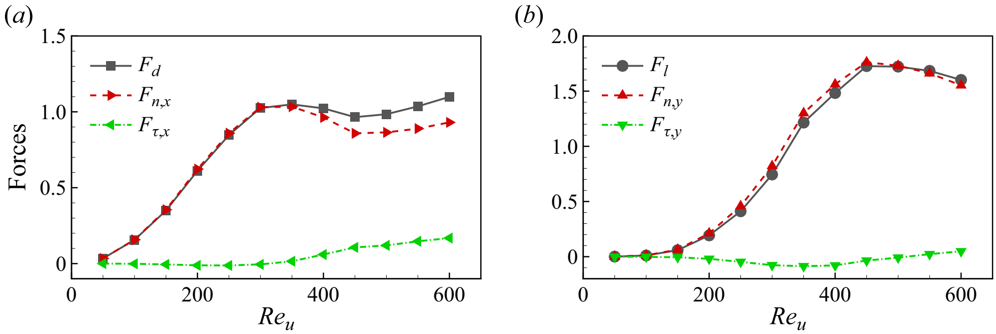

Figure 12. (*a*) The drag F_d, the total x-component of $\boldsymbol{f}_n$ and $\boldsymbol{f}_\tau$ (i.e. $F_{n,x}$ and $F_{\tau,x}$) and (*b*) the lift F_l, the total y-component of $\boldsymbol{f}_n$ and $\boldsymbol{f}_\tau$ (i.e. $F_{n,y}$ and $F_{\tau,y}$) as functions of Re_u with $M_t = 2$. The forces are rescaled using G.

since $F_d \approx F_{n,x}$ and $F_{\tau,x} \approx 0$ (see figure 12*a*). When $Re_u > 300$, the tangential force begins to exert its effect in generating drag, contributing approximately 15 % of the drag for $Re_u = 600$ (see figure 12*a*). These results are consistent with our estimation of skin friction or tangential force in § 4.1.1. Therefore, for high Re_u (or θ_l), the drag calculated by the theoretical model (4.5) is smaller than the actual one (see figure 11*a*).

On the other hand, as shown in figure 12(*b*), the tangential force contributes less to the lift, and almost all the lift is generated by the normal force, i.e. $F_l \approx F_{n,y}$. Hence, the theoretical model works well for the lift, even when Re_u (or θ_l) is large (see figure 11*b*).

4.1.3. *Normalization analysis and rescaling*

In § 4.1.1, we presented key results of the ribbons vs Re_u, normalizing the forces by $F_{ref} = (1/2)\rho U_{ref}^2 L$. However, these data did not collapse (see figure 7). The introduction of new scaling parameters is necessary to achieve a possible uniform scaling and enhance our understanding of the underlying mechanisms of the problem.

Note that the forces involved in the system mainly include the fluid force characterized by $\rho U^2 L$, the elastic force characterized by EI/L^2 and the weight G added at the trailing edge. Since the bending stiffness of the ribbon in our study is $K = EI/\rho U_{ref}^2 L^3 = 10^{-4}$, we can see that $EI/L^2 = 10^{-4}\rho U_{ref}^2 L \approx 10^{-4}\rho U^2 L$, i.e. the elastic force is negligible because it is much smaller than the fluid force. While G and $\rho U^2 L$ are of the same order of magnitude. Therefore, the behaviour of the ribbon is primarily governed by the balance between G and the characteristic fluid force $\rho U^2 L$. Hence, a key non-dimensional parameter can be defined as (Barois & de Langre 2013)

$$C_G = \frac{\rho U^2 L}{2G}, \tag{4.9}$$

which can also be regarded as the G-normalized characteristic fluid force. It is inspired by the theoretical model in § 4.1.2, where f_n, F_d and F_l are all proportional to G (see (4.4), (4.5) and (4.6)). This suggests that G serves as the characteristic force of the system, and all forces, including the characteristic fluid force $\rho U^2 L$, should be rescaled using G.

The forces and angle data in the new scaling are plotted in figure 13. Remarkably, this scaling collapses the data well for all M_t, compared with figure 7. Additionally, for small C_G, the G-normalized drag can be scaled as $F_d/G \sim C_G$, corresponding to the U^2 growth

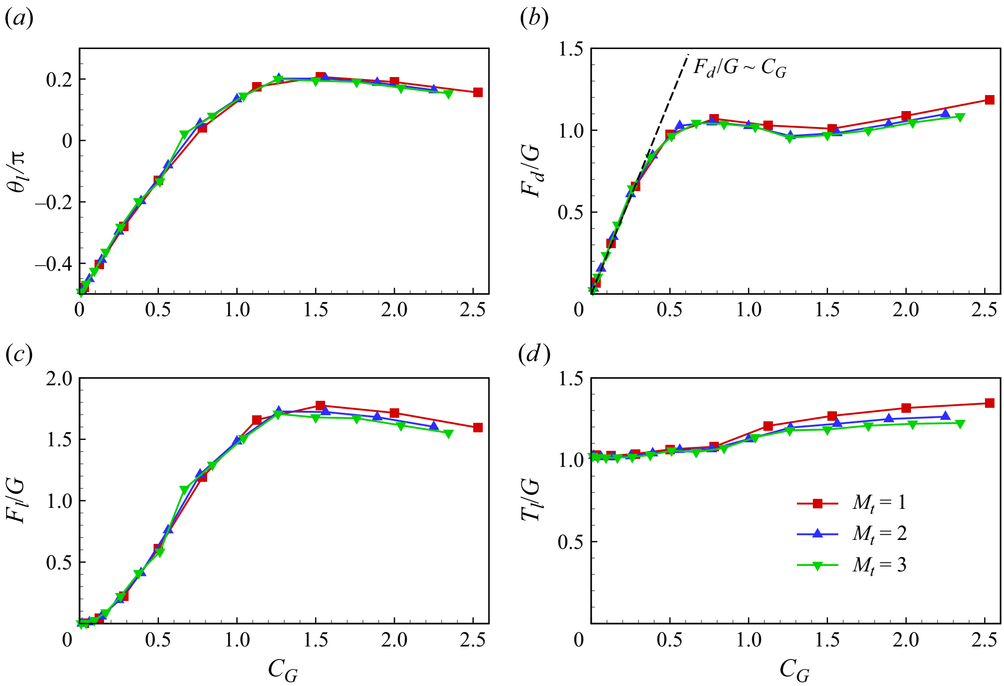

Figure 13. (*a*) Leading-edge inclination angle θ_l, (*b*) drag F_d, (*c*) lift F_l and (*d*) leading-edge tension T_l as functions of C_G for various M_t.

of drag in figure 7(*b*); while $F_d/G \approx 1$ when C_G is large (see figure 13*b*), corresponding to $F_d \approx G$ (figure 7*b*). It is also noteworthy that, similar to Re_u^c, there is a critical C_G, i.e. C_G^c, beyond which the system is unstable due to self-collision of the ribbon. For various M_t, C_G^c remains almost constant, at approximately 2.4 (see figure 13). This consistency suggests that C_G^c effectively characterizes the system, offering a more stable descriptor than Re_u^c, which increases with M_t. Hence, C_G proves to be a more suitable control parameter for the system.

4.1.4. *Vortex-induced vibration of the ribbon*

In the following, we will discuss the details of the VIV observed in the ribbons (Williamson & Govardhan 2004). Figure 14 presents the instantaneous vorticity contours and corresponding power spectrum density of the transverse force for $Re_u = 200$, 300 and 500 with $M_t = 2$. The flow behind the ribbon exhibits unsteadiness, with vortices shedding alternately, forming a classical Kármán vortex street (see supplementary movies available at https://doi.org/10.1017/jfm.2024.512). The vortex shedding frequency corresponds to the dominant frequency of the transverse force, denoted as f_1, or the vibration frequency of the ribbon. Observing figure 14(*b*,*d*,*f*), it is evident that f_1 increases with the rise in Re_u. The increase in vortex shedding frequency f_1 signifies a reduction in the streamwise distance between adjacent vortices. Additionally, as Re_u increases, the transverse projected length of the ribbon L_y gradually decreases (see figure 6*b*), resulting in a narrower wake. Consequently, for larger Re_u, the vortex street tends to be more compact in both the streamwise and transverse directions, as illustrated in figure 14(*a*,*c*,*e*). Furthermore, it is observed that, at relatively large Re_u (e.g. $Re_u = 500$ in figure 14*e*), the vortex street appears irregular. This irregularity may be attributed to the complex interaction between

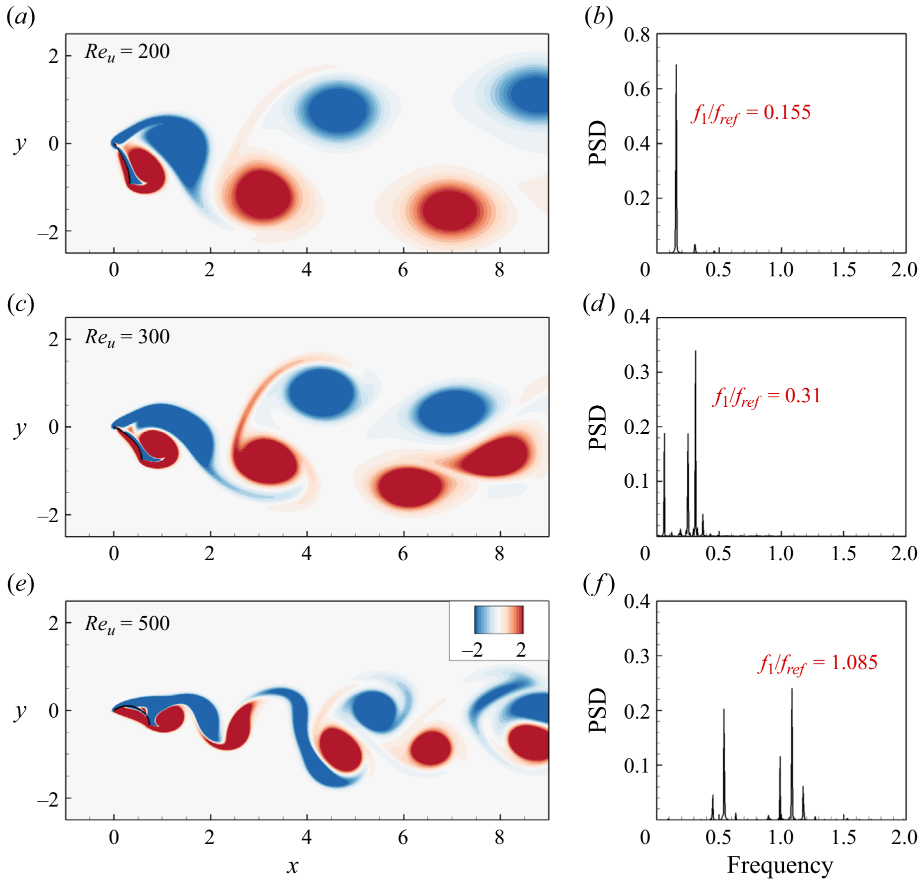

Figure 14. Instantaneous vorticity contours (*a*,*c*,*e*) and corresponding power spectrum density (PSD) of the transverse force (*b*,*d*,*f*) for (*a*,*b*) $Re_u = 200$, (*c*,*d*) $Re_u = 300$ and (*e*,*f*) $Re_u = 500$ with $M_t = 2$. The frequency is normalized by $f_{ref} = U_{ref}/L$.

the ribbon's structure and the vortices, leading to the emergence of secondary frequencies, as depicted in figure 14(*f*).

Note that the first natural frequency of the ribbon in vacuum is given by: $f_1^{vac} = (C_1^2/2\pi L^2)\sqrt{EI/\rho_s h} = U_{ref}/L \cdot (C_1^2/2\pi)\sqrt{K/M}$, where $C_1 = 1.875$ is a constant (Van Eysden & Sader 2006). Thus, the dimensionless first natural frequency is represented as $\hat{f}_1^{vac} = f_1^{vac} \cdot L/U_{ref} = (C_1^2/2\pi)\sqrt{K/M}$. In our study, the bending stiffness K ($= 10^{-4}$) is very small and the mass ratio M is of the order of 1. Consequently, $\hat{f}_1^{vac}$ is considerably small, nearly two orders of magnitude smaller than the observed flapping frequency in figure 14. In conventional VIV systems, such as an elastically mounted rigid cylinder, the oscillation frequency of the body closely aligns with its natural frequency f_1^{vac} (Williamson & Govardhan 2004). This is attributed to the significant value of K, where the elastic force acts as the primary restoring force for body vibration. However, in our study, the elastic force EL/L^2 is negligible compared with the fluid force (see § 4.1.3). In the following, we will demonstrate that the Strouhal number (St) related to the ribbon's vibration frequency is determined by the equilibrium between the fluid reaction force and pressure difference moments.

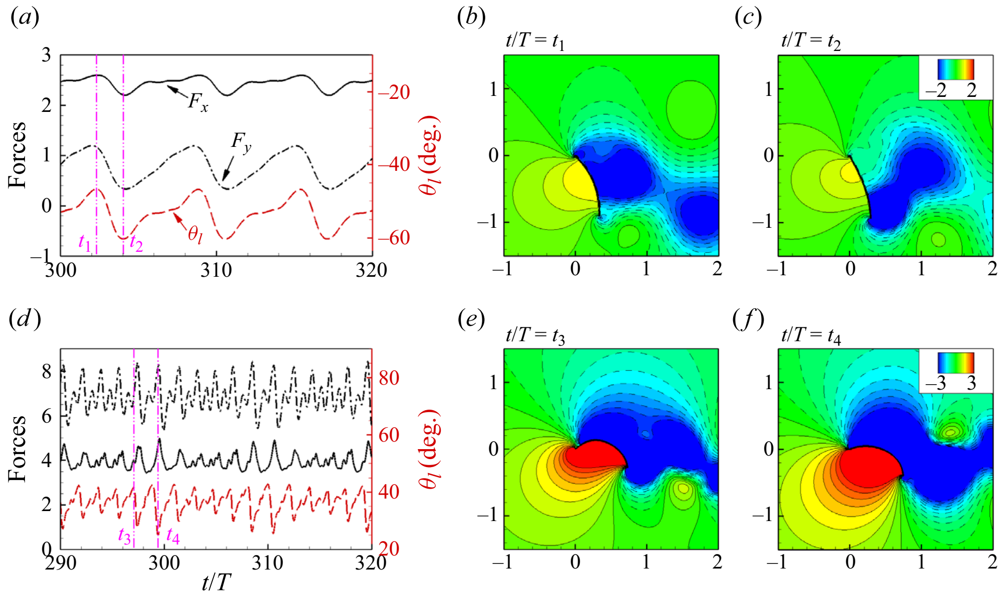

Figure 15. Time history of streamwise force F_x, transverse force F_y and leading edge inclination angle θ_l for (*a*) case I: $M_t = 2$, $Re_u = 200$ and (*d*) case II: $M_t = 2$, $Re_u = 500$. (*b*,*c*) Instantaneous pressure contours in case I. (*e*,*f*) Instantaneous pressure contours in case II. At $t = t_1$ and t_3, the ribbons reach their maximum θ_l; at $t = t_2$ and t_4, minimum θ_l. Solid and dashed lines for pressure contours denote the positive and negative normalized pressure contours.

Vortex shedding induces time-varying forces on the ribbons, as shown in figure 15, which illustrates the time history of forces (F_x and F_y), θ_l and instantaneous pressure contours at several representative moments. In the case with a lower Re_u (i.e. case I: $Re_u = 200$ in figure 15*a*), the forces and θ_l exhibit an in-phase relationship. Specifically, when θ_l reaches its local maximum value at $t/T = t_1$, the high pressure difference across the ribbon (see figure 15*b*) results in large F_x and F_y. Conversely, when θ_l is at its local minimum, i.e. $t/T = t_2$, the pressure difference across the ribbon significantly diminishes (see figure 15*c*), leading to lower F_x and F_y at that instant.

However, in the case with a higher Re_u (i.e. case II: $Re_u = 500$ in figure 15*d*), the forces and θ_l exhibit an antiphase relationship. At $t/T = t_3$, high pressure exists near the leading edge (figure 15*e*), causing the ribbon to lift upwards and θ_l to reach a local maximum value. Conversely, at $t/T = t_4$, the high-pressure range extends backward and downward (figure 15*f*), corresponding to a locally minimum θ_l (figure 15*d*). It is worth noting that a smaller θ_l implies a large transverse projected length L_y and higher pressure difference. As a result, the locally minimum θ_l at $t/T = t_4$ leads to larger forces (F_x and F_y) compared with those at $t/T = t_3$ (see figure 15*e*,*f*). Additionally, due to the superposition of multiple frequencies (see figure 14*f*), the variation of forces with time at $Re_u = 500$ is more complex than at $Re_u = 200$.

Furthermore, the time-varying forces induce significant vibrations of the flexible ribbon. In this context, the Strouhal number St, based on the vibration frequency f_1, ribbon length L and inflow speed U, can be introduced (Shelley *et al.* 2005; Huang & Sung 2010), i.e.

$$St = \frac{f_1 L}{U}. \tag{4.10}$$

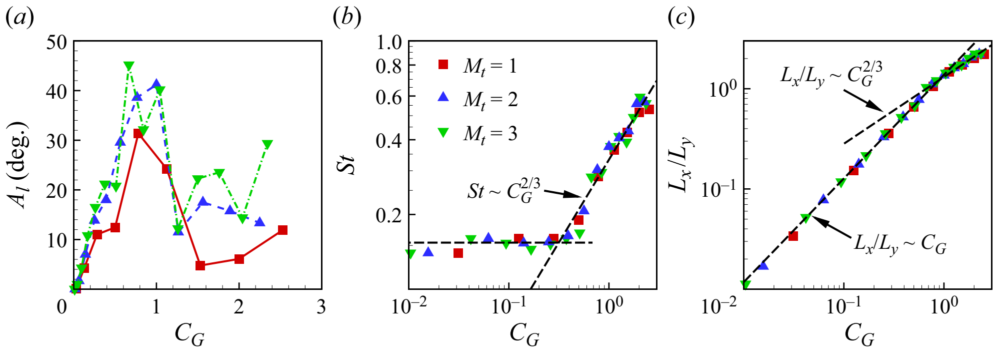

Figure 16. (*a*) The leading-edge vibration amplitude A_l, (*b*) the Strouhal number St and (*c*) L_x/L_y for different M_t as functions of C_G.

Besides, the leading-edge vibration amplitude A_l can be defined as the difference between the maximum and minimum values of the leading-edge inclination angle θ_l. The values of A_l and St as functions of C_G for various M_t are presented in figure 16(*a*,*b*). It is observed that, as C_G increases, A_l significantly grows due to the effects of vortex shedding, reaching a maximum of 30°–45° (see figure 16*a*). Meanwhile, it is surprising to find that St remains almost constant, i.e. $St = C$ for small C_G, where $C \approx 0.154$ is a constant (see figure 16*b*). In the following, we will show that this behaviour can be interpreted by considering the balance of moments on the ribbon.

During the ribbon's vibration, the mass and acceleration of the surrounding fluid set into motion are scaled as ρL^2 and $f_1^2 L$, respectively (Batchelor 1967; Gazzola, Argentina & Mahadevan 2014). Consequently, the moment of the reaction force exerted by the fluid on the ribbon scales as $M_{rea} = \rho L^2 \cdot f_1^2 L \cdot L$, considering that the arm of the force is scaled as L. On the other hand, the moment caused by the pressure difference across the ribbon scales as $M_{pre} = F_{pre} L = (\rho U^2 L) \cdot L$, where F_{pre} is the force generated by the pressure difference. Balancing these two moments yields

$$f_1 L \sim U \quad \text{or} \quad St = C, \tag{4.11}$$

meaning that the vibration velocity of the trailing edge $f_1 L$ is proportional to U, and consequently, St remains unchanged for small C_G.

Next, we would like to focus on the range of large C_G. As C_G further increases, A_l significantly decreases while St notably increases (see figure 16*a*,*b*). In this case, a simple scaling law between St and C_G emerges, namely $St \sim C_G^{2/3}$ (see figure 16*b*). The explanation for this behaviour is analogous to the earlier analysis. For large C_G (i.e. large U or Re_u), the ribbon experiences an overall upward lift and bending deformation (figure 5). Consequently, the acceleration of the surrounding fluid and the arm of the force are scaled as $f_1^2 L_y$ and L_y, respectively. This leads to M_{rea} being scaled as $\rho L^2 \cdot f_1^2 L_y \cdot L_y$. On the other hand, the moments of streamwise and transverse forces caused by pressure difference are scaled as $M_{pre,s} = \rho U^2 L_y \cdot L_y$ and $M_{pre,t} = \rho U^2 L_x \cdot L_x$, respectively. Note that $M_{pre,s}$ may be small enough to be ignored since L_y is much smaller than L_x when Re_u (or C_G) is large (see figure 6). Balancing the moments M_{rea} and $M_{pre,t}$, we obtain

$$f_1 L \cdot L_y \sim U \cdot L_x \quad \text{or} \quad St \sim L_x/L_y, \tag{4.12}$$

meaning that St is proportional to L_x/L_y. Figure 16(*c*) shows L_x/L_y as a function of C_G. It is observed that, for large C_G, L_x/L_y exhibits approximately $C_G^{2/3}$ growth.

Hence, (4.12) becomes

$$St \sim L_x/L_y \sim C_G^{2/3}, \tag{4.13}$$

which aligns well with the St-scaling indicated in figure 16(b) for large C_G.

Additionally, when C_G is small, L_x/L_y demonstrates a more rapid growth (figure 16c), i.e.

$$L_x/L_y \sim C_G \sim U^2, \tag{4.14}$$

attributed to the gradually noticeable deformations of the ribbon as the speed increases (see figure 6). Note that the transitions of the St- and Lx/Ly-scalings both occur around $C_G \approx 0.5$ (see figure 16b,c), indicating a strong correlation between them.

It is noteworthy that the range of St in the present study agrees broadly with that observed in prior research on flapping flexible bodies (Taylor *et al.* 2003; Shelley *et al.* 2005; Connell & Yue 2007; Huang & Sung 2010), specifically falling within $St \in [0.15, 0.6]$. Moreover, considering $St \sim C_G^{2/3} \sim U^{4/3}$, it follows that $f_1 \sim U^{7/3}$, implying a rapid increase in f_1 with increasing U. In simpler terms, the ribbon undergoes high-frequency vibration when U (or Re_u) is large. This high-frequency vibrational state is inherently unstable and can potentially result in self-collision of the ribbon. As discussed in §§ 4.1.1 and 4.1.3, critical values of Re_u and C_G (i.e. Re_u^c and C_G^c) exist, below which the system remains stable.

4.2. *Analysis of three-dimensional results*

In the preceding discussions of 2-D ribbon simulations, we uncovered significant differences compared with the results obtained from the 3-D experiments conducted by Barois & de Langre (2013), such as the uplift of ribbons ($\theta_l > 0$) at high Re_u and the emergence of the VIV phenomenon. To elucidate the underlying reasons for these phenomena and gain a deeper understanding of the distinctions between 2-D simulations and 3-D experiments, we conducted 3-D simulations of the ribbons. In this context, we primarily focused on exploring the influences of the aspect ratio AR (set to values of 0.25, 0.5 and 1) and inflow Reynolds number Re_u (ranging from 50 to 600 with intervals of 50), while maintaining $M_t = 1$. The following sections provide a detailed examination of the reconfiguration, forces acting on the ribbons, and the associated flow fields in the context of these 3-D simulations.

4.2.1. *Reconfiguration and forces*

In the present 3-D simulations, the ribbon undergoes primarily chordwise bending deformations, exhibiting minimal twisting or spanwise bending deformations. The ribbon profile remains almost identical at different spanwise positions. Figure 17 presents the equilibrium configurations of ribbons on the $z = 0$ section (symmetry plane), showing a gradual upward deflection as U (or Re_u) increases, similar to the 2-D results (see figure 5 or the dashed lines in figure 17a). An intriguing observation is that, in the case of 3-D ribbons, θ_l experiences a significant reduction (figure 17), particularly when AR is small. This reduction is more apparent in figure 18(a), which depicts θ_l as a function of Re_u for various AR. Specifically, for $\mathit{AR} = 1$, the maximum value of θ_l (i.e. $\theta_{l,max}$) is 22.6°; for $\mathit{AR} = 0.5$, $\theta_{l,max} = 13.6°$; while for $\mathit{AR} = 0.25$, $\theta_{l,max} = 4.7°$ (see figure 18a), which is notably small. It is worth noting that, for the 2-D ribbons with $\mathit{AR} = \infty$, $\theta_{l,max}$ reaches up to 36° (see figures 18(a) or 7(a)). Therefore, as AR decreases, $\theta_{l,max}$ tends to approach zero, consistent with experimental findings by Barois & de Langre (2013) where $\mathit{AR} \approx 0.1$ for

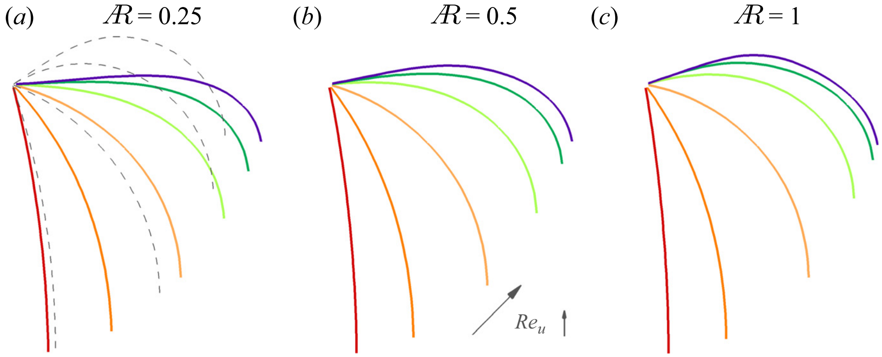

Figure 17. The equilibrium configurations of ribbons on the $z = 0$ section (symmetry plane) for (*a*) $Æ = 0.25$, (*b*) $Æ = 0.5$ and (*c*) $Æ = 1$ with Re_u ranging from 100 to 600. Each curved line represents the equilibrium state of a case. If the ribbon exhibits periodic oscillation, i.e. when the leading-edge vibration amplitude A_l is non-zero (refer to figure 21), the curve represents a time-averaged configuration. From bottom to top, Re_u gradually increases in increments of 100. For comparison, the equilibrium configurations of the 2-D ribbon (i.e. the dashed lines) for $M_t = 1$ and $Re_u = 100$–400 (as shown in figure 5*a*) are also presented in (*a*).

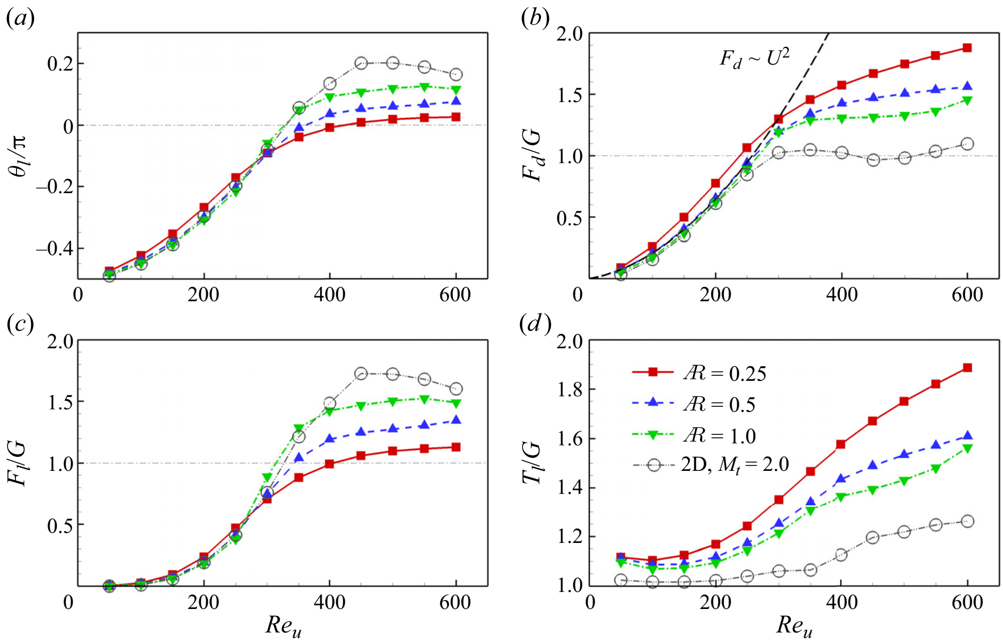

Figure 18. (*a*) Leading-edge inclination angle θ_l, (*b*) drag F_d, (*c*) lift F_l and (*d*) leading-edge tension T_l of the 3-D ribbons as functions of Re_u for various Æ. For comparison, the corresponding 2-D results with $M_t = 2$ are also presented, see the double dots lines.

rectangular ribbons resulted in $\theta_{l,max} = 0^\circ$. This phenomenon is attributed to 3-D effects, as elaborated in § 4.2.3.

The forces (i.e. F_d, F_l and T_l) for various Æ are also displayed in figure 18. It can be observed that, similar to the 2-D results in figures 18(*b*) or 7(*b*), when Re_u is small, the 3-D ribbon's F_d is well approximated by U^2 growth due to the small deformations (figure 18*b*). However, as Re_u increases further, F_d continues to rise at a reduced rate,

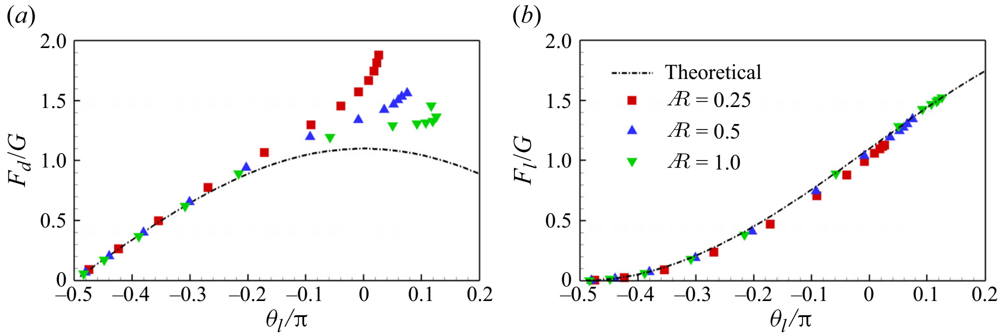

Figure 19. The G-normalized (*a*) drag F_d/G and (*b*) lift F_l/G as functions of θ_l for various $\mathcal{R}$. The dash-dotted lines are the theoretical lines given by (4.5) and (4.6).

ultimately surpassing the weight G (figure 18*b*). This increase is attributed to the drag contributed by skin friction or tangential force, which is evident in figure 18(*d*), where T_l/G significantly exceeds 1. It is worth noting that when skin friction is negligible, $T_l/G \approx 1$.

Concerning the lift shown in figure 18(*c*), similar to the 2-D results, the changing trend of F_l aligns with that of θ_l (see figure 18*a*,*c*). Moreover, for narrow cases (i.e. $\mathcal{R} = 0.25$) and large Re_u, the G-normalized lift $F_l/G \approx 1$ (see figure 18*c*) since $\theta_l \approx 0^\circ$, considering that $F_l = T_l \sin\theta_l + G$.

It is essential to note that all the data in figure 18 closely depend on $\mathcal{R}$, a key parameter determining 3-D effects. For wide ribbons, the results will be akin to those of 2-D cases (see figure 18); for instance, θ_l for $\mathcal{R} = 1$ closely resembles the 2-D data (see figure 18*a*). However, for narrow cases, the ribbons exhibit higher F_d/G and T_l/G but lower F_l/G and θ_l. Due to these opposing effects, introducing a single correction parameter that can collapse all the data proves challenging. In the subsequent sections (§§ 4.2.2 and 4.2.3), we will focus on the 3-D effects in detail by analysing the flow field.

To assess the suitability of the theoretical model in 3-D scenarios, we examine the G-normalized drag F_d/G and lift F_l/G as functions of θ_l for various $\mathcal{R}$ in figure 19. Similar to the 2-D results in figure 11(*b*), the theoretical model accurately predicts the lift F_l for all 3-D cases (see figure 19*b*). However, for the drag, the theoretical model proves accurate only within a narrower range of θ_l or Re_u (see figure 19*a*) and when θ_l or Re_u is large, a significant discrepancy emerges between theoretical and simulated values of F_d, particularly for narrow ribbons (figure 19*a*). In 3-D cases, the theoretical model does not perform as well as it does in 2-D cases.

We aim to explore the potential reasons for this observation. We present the drag (F_d), lift (F_l) and the total x- and y-components of normal and tangential forces ($F_{n,x}$, $F_{\tau,x}$, $F_{n,y}$ and $F_{\tau,y}$) as functions of Re_u for $\mathcal{R} = 0.25$ in figure 20. The analysis reveals a substantial increase in the drag provided by the tangential force (i.e. $F_{\tau,x}$) at high Re_u. For instance, at $Re_u = 600$ and $\mathcal{R} = 0.25$, $F_{\tau,x}$ constitutes 39 % of the total drag F_d (see figure 20*a*), whereas it accounts for only approximately 15 % at most in the 2-D cases (see figure 12*a*). A plausible explanation for the elevated tangential force or skin friction at small $\mathcal{R}$ is as follows. When $\mathcal{R} = 0.25$ and Re_u is large, the front and middle portions of the ribbons are oriented horizontally (see figure 17*a*). In this configuration, the direction of the tangential force is parallel to that of F_d, implying that all the tangential force contributes to drag. Conversely, in the case of 2-D ribbons or 3-D ribbons with larger $\mathcal{R}$, where the body curves upwards (see figures 5 and 17*b*,*c*), only the x-component or a portion of the

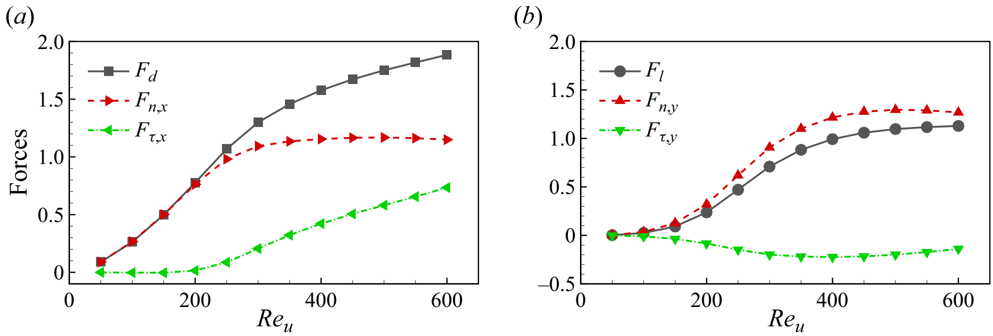

Figure 20. (*a*) The drag F_d, the x-component of $\boldsymbol{f}_n$ and $\boldsymbol{f}_\tau$ (i.e. $F_{n,x}$ and $F_{\tau,x}$) and (*b*) the lift F_l, the y-component of $\boldsymbol{f}_n$ and $\boldsymbol{f}_\tau$ (i.e. $F_{n,y}$ and $F_{\tau,y}$) as functions of Re_u with $\mathcal{R} = 0.25$. The forces are normalized by G.

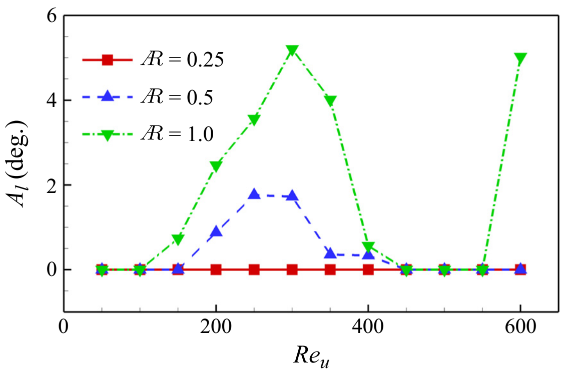

Figure 21. The leading-edge vibration amplitude A_l of the 3-D ribbons as a function of Re_u for various $\mathcal{R}$.

tangential force contributes to drag. Consequently, for narrow cases (i.e. $\mathcal{R} = 0.25$), the tangential force contributes a higher proportion to drag. It is noteworthy that the tangential force is disregarded in the theoretical model, leading to a smaller theoretical value for drag compared with F_d. This difference is more pronounced for narrow ribbons (see figure 19*a*). The equilibrium configuration is associated with the fluid flow and pressure on the ribbon, which will be discussed in detail in § 4.2.3.

For the lift, as shown in figure 20(*b*), it is observed that the tangential force generates a small negative lift contribution, denoted by $F_{\tau,y} < 0$, primarily due to the sagging of the trailing edge. Consequently, $F_{n,y}$ in figure 20(*b*) and the theoretical lift value in figure 19(*b*) are slightly larger than F_l. However, the negative lift is relatively small and decreases with the increase of $\mathcal{R}$. Therefore, the theoretical model performs exceptionally well in predicting the lift, particularly for wide ribbons, such as $\mathcal{R} = 1$ in figure 19(*b*).

4.2.2. *Three-dimensional effects stabilize ribbon motion*

The VIV phenomenon may also occur in 3-D scenarios. Figure 21 displays the leading-edge vibration amplitude A_l as a function of Re_u for various $\mathcal{R}$. It is evident that, in comparison with the 2-D results presented in figure 16, the vibrations of the 3-D ribbons are significantly suppressed, particularly for narrow cases. More specifically, at $Re_u = 300$, for $\mathcal{R} = 1$, the maximum value of A_l (i.e. $A_{l,max}$) is notably reduced to approximately 5°,

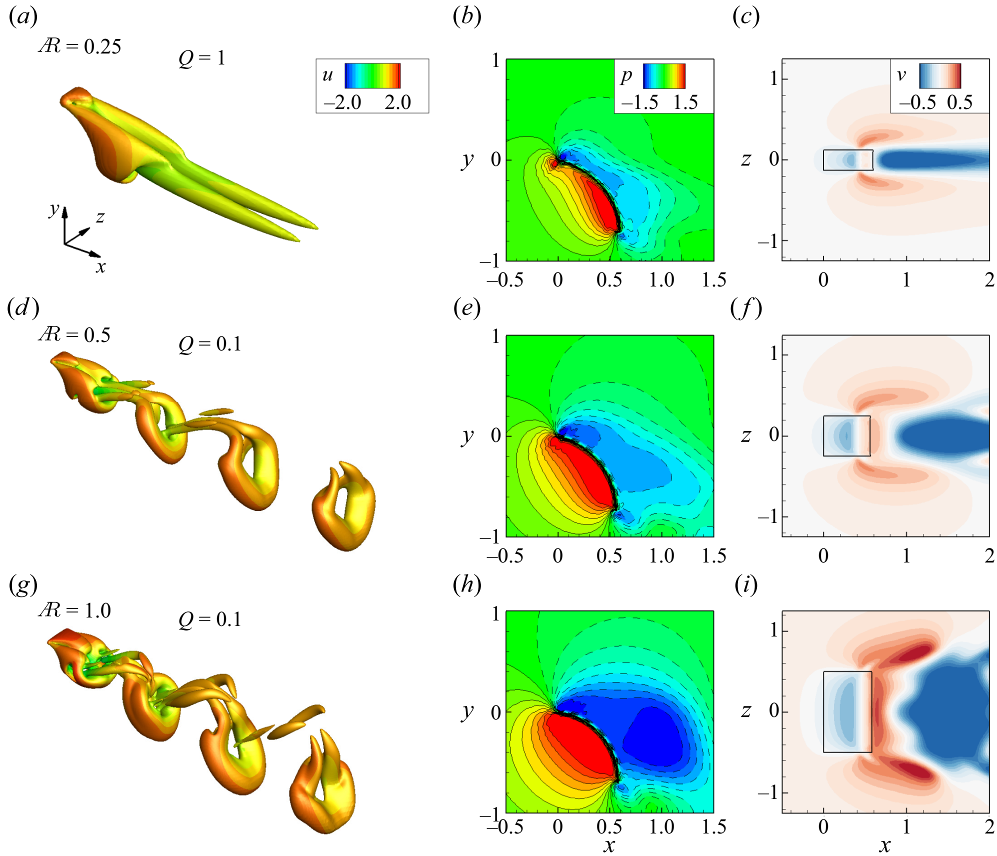

Figure 22. Snapshots of (*a*,*d*,*g*) vortical structures visualized by an isosurface of the Q criterion, (*b*,*e*,*h*) pressure contours at the spanwise symmetry plane $z = 0$ of the ribbon and (*c*,*f*,*i*) transverse velocity contours at the horizontal section $y = -0.3$ for the cases with $Re_u = 300$ (the top views of the ribbons are also drawn). From top row to bottom row, $\mathcal{R} = 0.25$, 0.5 and 1, respectively. The isosurface of the Q criterion is coloured by streamwise velocity u.

in contrast to the $A_{l,max} \approx 45^\circ$ observed for the 2-D cases. Here, $A_{l,max}$ generally decreases with $\mathcal{R}$: $A_{l,max} \approx 2^\circ$ and 0 for $\mathcal{R} = 0.5$ and 0.25, respectively (see figure 21). Hence, it appears that the 3-D effects contribute to making the ribbons more stable compared with their 2-D counterparts. Consequently, the St scalings observed for 2-D ribbons in figure 16(*b*) are no longer applicable in 3-D scenarios.

The vibration characteristics of the ribbons may be closely associated with flow structures. Figure 22 presents snapshots of the vortical structures around the ribbons visualized by an isosurface of the Q criterion, pressure contours at the spanwise symmetry plane $z = 0$ and transverse velocity contours at the horizontal section $y = -0.3$ for various $\mathcal{R}$ with $Re_u = 300$. In the cases of $\mathcal{R} = 0.5$ and 1, the snapshots are at the instant when θ_l is at its maximum. It is observed that the vortical structure for $\mathcal{R} = 0.25$ demonstrates a steady pattern with two long antennae extended downstream (figure 22*a*). In contrast, for $\mathcal{R} = 0.5$ and 1, there is regular shedding of a hairpin-shaped vortex structure due to the vibration of the ribbon (see figure 22(*d*,*g*) or supplementary movies). Moreover, the vortical structure for larger $\mathcal{R}$ (i.e. $\mathcal{R} = 1$) appears stronger than that for smaller $\mathcal{R}$ (i.e. $\mathcal{R} = 0.5$). These differences can be explained by analysing the velocity and

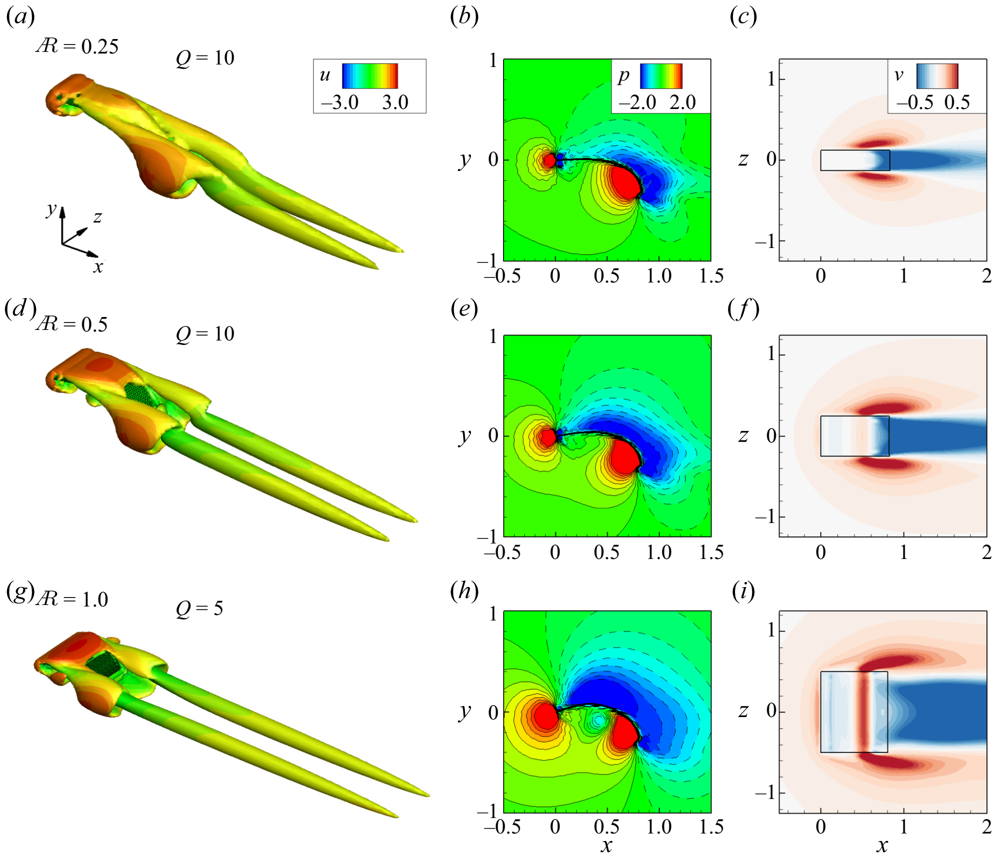

Figure 23. Same as figure 22, but $Re_u = 500$ and the position of the horizontal section for the transverse velocity contours (*c*,*f*,*i*) is $y = 0$.

pressure fields. Examination of the velocity and pressure fields reveals that the fluid near the two side edges of the ribbon exhibits a significant upward velocity (see figure 22(*c*,*f*,*i*), where the transverse velocity $v > 0$ near the two sides). In other words, the flow can leak from the two side edges, alleviating the high pressure below the ribbons and decreasing the pressure difference across the ribbon (Gosselin *et al.* 2010), especially for cases with small Æ. As shown in figure 22(*b*,*e*,*h*), the pressure difference across the ribbon is clearly reduced as Æ decreases, further suppressing the generation and shedding of vortices. Consequently, when Æ $= 0.25$, the boundary layer is completely attached to the ribbon without flow separation (figure 22*a*). In summary, the leakage of flow from the two sides of the ribbon is a key 3-D effect mechanism that stabilizes the ribbon's motion.

4.2.3. *Three-dimensional equilibrium configuration and fluid flow*

For cases with larger Re_u (i.e. $Re_u > 300$), the vibration amplitude A_l of the ribbon decreases, and in some instances, the ribbon does not vibrate at all (see figure 21). Figure 23 presents the corresponding vortical structures, pressure and velocity contours for $Re_u = 500$. It is evident that the fluid near the two sides exhibits larger transverse velocity (figure 23*c*,*f*,*i*), resulting in a significant reduction of the high-pressure region below the ribbon. For instance, in the narrow case (i.e. Æ $= 0.25$ in figure 23*b*), high pressure is concentrated mainly ahead of the leading and trailing edges, accompanied by a negative pressure distribution behind them, indicating a high pressure difference near the leading and trailing edges. This configuration is beneficial for increasing drag but not lift. It is also noted that the wider ribbon exhibits a broader range of positive and negative pressure regions compared with the narrow ribbon, resulting in a higher overall pressure difference. This leads to increased total drag (F_d) and lift (F_l) for the wider ribbon. However, it is important to consider the influence of the weight ($G = Wm_t g$) added at the trailing edge, which is proportionally larger for the wider ribbon due to its increased span length W. As a result, the narrower ribbon may achieve a higher drag-to-weight ratio (F_d/G) but a lower lift-to-weight ratio (F_l/G), as depicted in figure 18(*b*,*c*).

Additionally, for the front half of the ribbon, the pressure is nearly the same above and below due to flow leakage from the two sides, resulting in a very small corresponding pressure difference (figure 23*b*). As a result, the front half of the ribbon is approximately horizontal, implying $\theta_l \approx 0$ for large Re_u. This aligns well with our findings in figure 18(*a*) and the experimental results of Barois & de Langre (2013) for narrow ribbons. As $\mathcal{R}$ increases (i.e. $\mathcal{R} = 0.5$ and 1), the negative pressure range extends forward, and a considerable pressure difference across the front half of the ribbon is generated (figure 23*e*,*h*), causing the ribbon to bend upwards. Hence, for wide ribbons, θ_l is evidently greater than 0 when Re_u is large (see figure 18*a*).

From the above analysis, we observe that the effects of side edge flow leakage are more pronounced for high Re_u (i.e. $Re_u = 500$). Consequently, ribbons with different $\mathcal{R}$ remain stable, and the corresponding vortical structures are similar to those shown in figure 22(*a*) – a steady wake pattern with two long antennae (figure 23*a*,*d*,*g*). However, as the inflow speed (or Re_u) increases further, reaching a sufficiently high value, the pressure difference can induce instability in the system, overriding the stabilizing effect of the 3-D dynamics. This effect becomes more pronounced, particularly for wider ribbons. Hence, for the case with $\mathcal{R} = 1.0$ (green line in figure 21), the ribbon exhibits noticeable vibration at $Re_u = 600$, resulting in a peak value of the leading-edge vibration amplitude A_l.

5. Concluding remarks

In this study, we investigate the dynamics of 2-D and 3-D weighted flexible ribbons in a uniform flow. As Re_u or inflow speed U increases in the 2-D cases, ribbons are lifted, with θ_l rising and L_y decreasing. At small Re_u, $F_d \sim U^2$, and at high Re_u, bending deformations become pronounced. At higher Re_u, the skin friction gradually increases, compensating for the reduced form drag and $F_d \approx G$. To better understand the underlying mechanisms, a simplified theoretical model is established based on assumptions that the tangential force or skin friction is ignored and the normal force is approximately evenly distributed along the ribbon. Our simplified theoretical model accurately predicts lift and effectively predicts equilibrium shapes and drag. The scaling parameter C_G, first introduced by Barois & de Langre (2013), successfully collapses forces and angle data for all 2-D cases.

In 2-D scenarios, ribbons undergo significant vibrations, exhibiting VIV with frequency f_1 increasing alongside oncoming flow velocity. The Strouhal number $St = f_1 L/U$ follows scaling laws with respect to C_G: for small C_G, St is constant, and for large C_G, $St \sim C_G^{2/3}$, confirmed through an analysis of the balance between fluid reaction force and pressure difference moments.

In 3-D cases, ribbons experience chordwise bending without obvious spanwise deformations, maintaining similarity to 2-D shapes. The theoretical model effectively

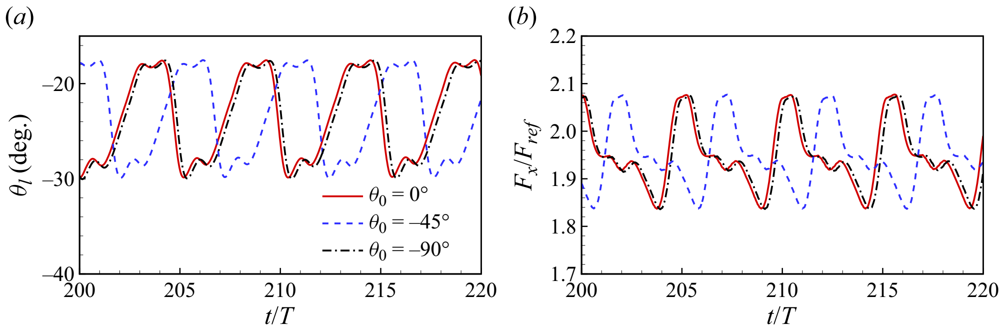

Figure 24. Time history of (*a*) leading-edge inclination angle θ_l and (*b*) streamwise force F_x of the 2-D ribbon for different θ_0 with $M_t = 1$ and $Re_u = 200$.

predicts lift, while drag, influenced by tangential force or skin friction, is accurately modelled for small Re_u only. Compared with 2-D ribbons, 3-D vibrations are suppressed. Side edge flow leakage effects reduce the pressure difference across ribbons, enhancing stability, particularly for narrow ribbons. This prevents uplift in narrower ribbons, keeping the front half nearly horizontal ($\theta_l \approx 0$) at large Re_u, consistent with prior experimental results. These insights contribute to a deeper understanding of the flexible body dynamics in a uniform flow.

Supplementary movies. Supplementary movies are available at https://doi.org/10.1017/jfm.2024.512.

Acknowledgements. Calculations are performed at the Supercomputing Center of the University of Science and Technology of China.

Funding. This work was supported by the Natural Science Foundation of China (NSFC) grant nos 11972342 and 11772326.

Declaration of interests. The authors report no conflict of interest.

Author ORCIDs.
Kui Liu https://orcid.org/0000-0001-9897-6375;
Haibo Huang https://orcid.org/0000-0002-1308-9900.

Appendix A. Initial angle independence

For the study on initial angle independence, we conducted tests with three different initial angles: $\theta_0 = 0°$, $-45°$ and $-90°$, corresponding to the initial horizontal, inclined and vertical placement of ribbons, respectively. Figure 24 presents the time history of the leading-edge inclination angle θ_l and streamwise force F_x for the 2-D ribbon with $M_t = 1$ and $Re_u = 200$ under different θ_0. It is observed that, despite a certain phase difference, the mean, amplitude and period of θ_l and F_x remain identical for different θ_0. We have also conducted tests for the 3-D cases (not shown here), and the results were consistent. Therefore, in our simulations, we set θ_0 to $-90°$, representing the natural drooping state.

Appendix B. Simplified theoretical model based on force decomposition

To establish a simplified model, we first decompose the force acting on the ribbon. As illustrated in figure 25(*a*), the Lagrangian force $\boldsymbol{f}_s$ exerted on the ribbon by the surrounding fluid can be broken down into two distinct components: the first is the normal force $\boldsymbol{f}_n$, where the pressure component predominantly contributes; the second is the tangential

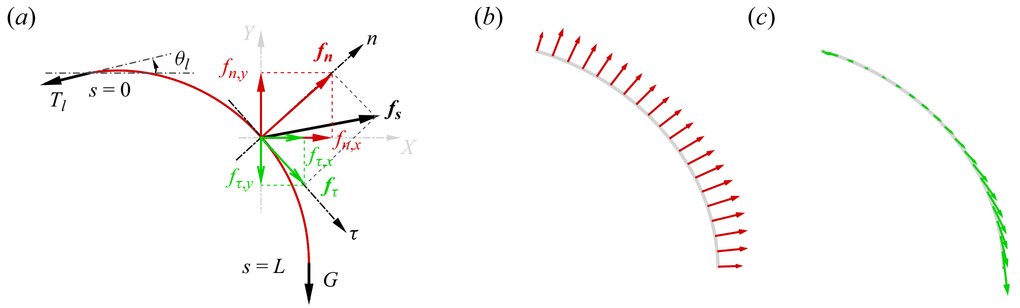

Figure 25. (*a*) Schematic diagram of force decomposition. Here, $\boldsymbol{\tau}$ and $\boldsymbol{n}$ denote the local tangential and normal vectors, respectively, θ_l is the leading-edge ($s = 0$) inclination angle, T_l is the leading-edge tension and G is the weight added at the trailing edge ($s = L$). (*b*,*c*) Depict the distributions of normal and tangential forces on the ribbon, respectively, with $M_t = 2$ and $Re_u = 350$.

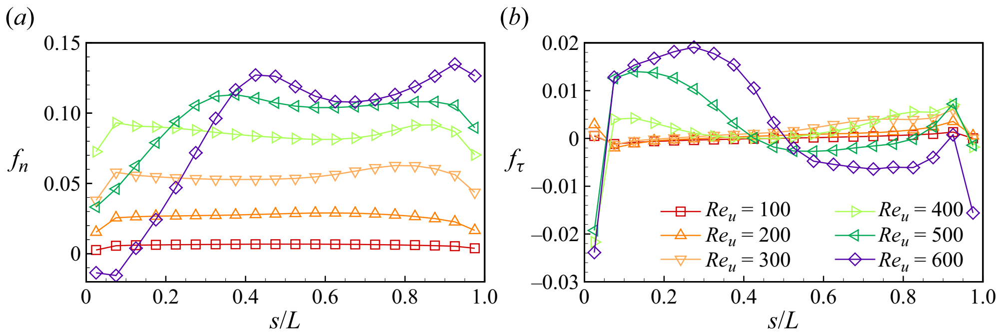

Figure 26. Distributions of (*a*) normal force f_n and (*b*) tangential force f_τ along the ribbon for various Re_u with $M_t = 2$.

force $\boldsymbol{f}_\tau$, primarily arising from viscous effects. The definitions of these forces are as follows (Peng, Huang & Lu 2018; Liu, Huang & Lu 2020; Liu *et al.* 2022):

$$\boldsymbol{f}_s = [-p\boldsymbol{I} + \boldsymbol{T}_\mu] \cdot \boldsymbol{n} = \boldsymbol{f}_n + \boldsymbol{f}_\tau, \tag{B1}$$

$$\boldsymbol{f}_n = (\boldsymbol{f}_s \cdot \boldsymbol{n})\boldsymbol{n} = f_n\boldsymbol{n} = (f_{n,x}, f_{n,y}), \tag{B2}$$

$$\boldsymbol{f}_\tau = (\boldsymbol{f}_s \cdot \boldsymbol{\tau})\boldsymbol{\tau} = f_\tau\boldsymbol{\tau} = (f_{\tau,x}, f_{\tau,y}), \tag{B3}$$

where $\boldsymbol{I}$ represents the unit tensor, $\boldsymbol{T}_\mu$ stands for the viscous stress tensor, f_n and f_τ denote the magnitudes of $\boldsymbol{f}_n$ and $\boldsymbol{f}_\tau$, respectively. Additionally, $\boldsymbol{\tau}$ indicates the unit tangential vector directed towards the trailing edge, $\boldsymbol{n}$ represents the unit normal vector and $[\cdot]$ signifies the jump in a quantity across the immersed boundary. As an illustrative example, figure 25(*b*,*c*) shows the distributions of normal and tangential forces on the ribbon, respectively, for $M_t = 2$ and $Re_u = 350$.

Figure 26 displays the normal and tangential forces (f_n and f_τ) along the ribbon for various Re_u with $M_t = 2$. It is evident that f_n generally increases with the rise in Re_u (figure 26*a*). This is attributed to a larger oncoming flow speed U, resulting in an increased pressure difference, as the pressure difference across the ribbon scales with ρU^2 (Ristroph & Zhang 2008; Gao *et al.* 2020). Moreover, when Re_u is not excessively large, f_n is approximately evenly distributed along the ribbon, except near the edges. Regarding the tangential force f_τ, it is notably small for $Re_u \leq 400$ and becomes relatively large for larger

Re_u (figure 26*b*). Consequently, skin friction or f_τ is negligible for small Re_u but may play a role for larger Re_u, consistent with our analysis in figure 7.

For higher Re_u, the trends of f_n and f_τ are closely linked to θ_l. Notably, the pressure contours around the ribbon for $Re_u > 400$ with $M_t = 2$ resemble those for $Re_u > 300$ with $M_t = 1$, as illustrated in figure 8. Consequently, as Re_u exceeds 400, the decrease in θ_l signifies a reduction in the pressure difference near the leading edge of the ribbon. This observation aligns with the significant decrease in f_n near the leading edge ($s/L = 0$) evident in figure 26(*a*), indicating an uneven distribution of f_n under these conditions. Furthermore, the decrease in θ_l coupled with the increase in Re_u promotes the generation of skin friction, resulting in a notable increase in the tangential force f_τ at higher Re_u values (figure 26*b*).

The preceding analysis lays the foundation for two key assumptions in establishing a simplified model, i.e. $f_n \approx C$ and $f_\tau \approx 0$, where C is a positive constant. However, it is crucial to note that these assumptions are valid only when Re_u is not excessively large.

Based on the force balance of a infinitesimal element, we can easily obtain the following equations about the normal and tangential forces (Barois & de Langre 2013):

$$T_s \frac{\mathrm{d}\theta}{\mathrm{d}s} = -f_n, \tag{B4}$$

$$\frac{\mathrm{d}T_s}{\mathrm{d}s} = -f_\tau, \tag{B5}$$

where T_s the local tension magnitude and θ is the local inclination angle of the ribbon. The negative sign in (B4) is attributed to the clockwise change in θ along the ribbon, which is opposite to the positive direction.

Since $f_\tau \approx 0$, (B5) becomes $\mathrm{d}T_s/\mathrm{d}s \approx 0$, which indicates that T_s is approximately constant. Considering the boundary condition at the trailing edge, i.e. $T_{s,s=L} = G$, we have $T_s \approx G$ along the ribbon. Therefore, (B4) is simplified as

$$\frac{\mathrm{d}\theta}{\mathrm{d}s} = -\frac{f_n}{G}, \tag{B6}$$

where the left side is the local curvature of the ribbon and the right side is a constant, i.e. (B6) represents a circular arc. The entire equilibrium shape of the ribbons with relatively small and moderate Re_u indeed resembles perfect circular arcs (see figure 5). Integrating (B6) and considering $\theta = -\pi/2$ at $\hat{s} = 1$ yields

$$\theta(\hat{s}) = -\frac{\pi}{2} + \frac{f_n L}{G}(1 - \hat{s}), \tag{B7}$$

where $\hat{s} = s/L$ is the dimensionless curvilinear coordinate along the ribbon, $f_n L$ represents the total normal force and $f_n L/G$ is the G-normalized total normal force. Equation (B7) is similar to the result of Barois & de Langre (2013). Further, in § 4.1.2, we demonstrate that the model can also be used to predict the forces on the ribbons.

REFERENCES

ALBEN, S. & SHELLEY, M. 2008 Flapping states of a flag in an inviscid fluid: bistability and the transition to chaos. *Phys. Rev. Lett.* **100**, 074301.

ALBEN, S., SHELLEY, M. & ZHANG, J. 2002 Drag reduction through self-similar bending of a flexible body. *Nature* **420**, 479–481.

ALBEN, S., SHELLEY, M. & ZHANG, J. 2004 How flexibility induces streamlining in a two-dimensional flow. *Phys. Fluids* **16**, 1694–1713.

ALLEN, J.J. & SMITS, A.J. 2001 Energy harvesting eel. *J. Fluids Struct.* **15** (3), 629–640.
BAROIS, T. & DE LANGRE, E. 2013 Flexible body with drag independent of the flow velocity. *J. Fluid Mech.* **735**, R2.
BATCHELOR, G.K. 1967 *An Introduction to Fluid Dynamics*. Cambridge University Press.
BUCHAK, P., ELOY, C. & REIS, P.M. 2010 The clapping book: wind-driven oscillations in a stack of elastic sheets. *Phys. Rev. Lett.* **105**, 194301.
CARLSON, D.W., CURRIER, T.M. & MODARRES-SADEGHI, Y. 2021 Flow-induced vibrations of a square prism free to oscillate in the cross-flow and inline directions. *J. Fluid Mech.* **919**, A2.
CHEN, S.Y. & DOOLEN, G.D. 1998 Lattice Boltzmann method for fluid flows. *Annu. Rev. Fluid Mech.* **30**, 329–364.
CONNELL, B.S.H. & YUE, D.K.P. 2007 Flapping dynamics of a flag in a uniform stream. *J. Fluid Mech.* **581**, 33–67.
DOYLE, J.F. 2001 *Nonlinear Analysis of Thin-Walled Structures: Statics, Dynamics, and Stability*. Springer.
ELOY, C., LAGRANGE, R., SOUILLIEZ, C. & SCHOUVEILER, L. 2008 Aeroelastic instability of cantilevered flexible plates in uniform flow. *J. Fluid Mech.* **611**, 97–106.
GAO, S., PAN, S., WANG, H. & TIAN, X. 2020 Shape deformation and drag variation of a coupled rigid-flexible system in a flowing soap film. *Phys. Rev. Lett.* **125**, 034502.
GAZZOLA, M., ARGENTINA, M. & MAHADEVAN, L. 2014 Scaling macroscopic aquatic locomotion. *Nat. Phys.* **10**, 758–761.
GOSSELIN, F., DE LANGRE, E. & MACHADO-ALMEIDA, B.A. 2010 Drag reduction of flexible plates by reconfiguration. *J. Fluid Mech.* **650**, 319–341.
HAN, P., DE LANGRE, E., THOMPSON, M.C., HOURIGAN, K. & ZHAO, J. 2023 Vortex-induced vibration forever even with high structural damping. *J. Fluid Mech.* **962**, A13.
HUA, R.-N., ZHU, L. & LU, X.-Y. 2013 Locomotion of a flapping flexible plate. *Phys. Fluids* **25**, 121901.
HUA, R.-N., ZHU, L. & LU, X.-Y. 2014 Dynamics of fluid flow over a circular flexible plate. *J. Fluid Mech.* **759**, 56–72.
HUANG, H., WEI, H. & LU, X.-Y. 2018 Coupling performance of tandem flexible inverted flags in a uniform flow. *J. Fluid Mech.* **837**, 461–476.
HUANG, W., SHIN, S.J. & SUNG, H.J. 2007 Simulation of flexible filaments in a uniform flow by the immersed boundary method. *J. Comput. Phys.* **226** (2), 2206–2228.
HUANG, W. & SUNG, H.J. 2010 Three-dimensional simulation of a flapping flag in a uniform flow. *J. Fluid Mech.* **653**, 301–336.
JIA, L.-B., LI, F., YIN, X.-Z. & YIN, X.-Y. 2007 Coupling modes between two flapping filaments. *J. Fluid Mech.* **581**, 199–220.
JIA, L.-B. & YIN, X.-Z. 2008 Passive oscillations of two tandem flexible filaments in a flowing soap film. *Phys. Rev. Lett.* **100**, 228104.
KIM, D., COSSÉ, J., HUERTAS CERDEIRA, C. & GHARIB, M. 2013 Flapping dynamics of an inverted flag. *J. Fluid Mech.* **736**, R1.
KIM, Y. & PESKIN, C.S. 2007 Penalty immersed boundary method for an elastic boundary with mass. *Phys. Fluids* **19** (5), 053103.
DE LANGRE, E. 2008 Effects of wind on plants. *Annu. Rev. Fluid Mech.* **40** (1), 141–168.
LAUDER, G.V. 2015 Fish locomotion: recent advances and new directions. *Annu. Rev. Mar. Sci.* **7**, 521–545.
LIU, K., HUANG, H. & LU, X.-Y. 2020 Hydrodynamic benefits of intermittent locomotion of a self-propelled flapping plate. *Phys. Rev.* E **102**, 053106.
LIU, K., LIU, X. & HUANG, H. 2022 Scaling the self-propulsive performance of pitching and heaving flexible plates. *J. Fluid Mech.* **936**, A9.
LUHAR, M. & NEPF, H.M. 2011 Flow-induced reconfiguration of buoyant and flexible aquatic vegetation. *Limnol. Oceanogr.* **56** (6), 2003–2017.
MATHAI, V., TZEZANA, G.A., DAS, A. & BREUER, K.S. 2022 Fluid–structure interactions of energy-harvesting membrane hydrofoils. *J. Fluid Mech.* **942**, R4.
NEPF, H.M. 2012 Flow and transport in regions with aquatic vegetation. *Annu. Rev. Fluid Mech.* **44** (1), 123–142.
O'CONNOR, J. & REVELL, A. 2019 Dynamic interactions of multiple wall-mounted flexible flaps. *J. Fluid Mech.* **870**, 189–216.
PENG, Z.-R., HUANG, H. & LU, X.-Y. 2018 Collective locomotion of two closely spaced self-propelled flapping plates. *J. Fluid Mech.* **849**, 1068–1095.
PLATZER, M.F., JONES, K.D., YOUNG, J. & LAI, J.C.S. 2008 Flapping wing aerodynamics: progress and challenges. *AIAA J.* **46** (9), 2136–2149.

RAISSI, M., WANG, Z., TRIANTAFYLLOU, M.S. & KARNIADAKIS, G.E. 2019 Deep learning of vortex-induced vibrations. *J. Fluid Mech.* **861**, 119–137.

RISTROPH, L. & ZHANG, J. 2008 Anomalous hydrodynamic drafting of interacting flapping flags. *Phys. Rev. Lett.* **101**, 194502.

SARPKAYA, T. 2004 A critical review of the intrinsic nature of vortex-induced vibrations. *J. Fluids Struct.* **19** (4), 389–447.

SCHOUVEILER, L. & BOUDAOUD, A. 2006 The rolling up of sheets in a steady flow. *J. Fluid Mech.* **563**, 71–80.

SCHOUVEILER, L. & ELOY, C. 2013 Flow-induced draping. *Phys. Rev. Lett.* **111**, 064301.

SHELLEY, M., VANDENBERGHE, N. & ZHANG, J. 2005 Heavy flags undergo spontaneous oscillations in flowing water. *Phys. Rev. Lett.* **94**, 094302.

SHELLEY, M. & ZHANG, J. 2011 Flapping and bending bodies interacting with fluid flows. *Annu. Rev. Fluid Mech.* **43** (1), 449–465.

SHEN, L., ZHANG, X., YUE, D.K.P. & TRIANTAFYLLOU, M.S. 2003 Turbulent flow over a flexible wall undergoing a streamwise travelling wave motion. *J. Fluid Mech.* **484**, 197–221.

SMITS, A.J. 2019 Undulatory and oscillatory swimming. *J. Fluid Mech.* **874**, P1.

SUN, Y., PENG, Z., YANG, D., XIONG, Y., WANG, L. & WANG, L. 2022 Dynamics of a rigid-flexible coupling system in a uniform flow. *J. Fluid Mech.* **943**, A44.

SUNIL, P., KUMAR, S. & PODDAR, K. 2022 Flow past a rotationally oscillating cylinder with an attached flexible filament. *J. Fluid Mech.* **930**, A3.

TANEDA, S. 1968 Waving motion of flags. *J. Phys. Soc. Japan* **24**, 392–401.

TAYLOR, G., NUDDS, R. & THOMAS, A. 2003 Flying and swimming animals cruise at a strouhal number tuned for high power efficiency. *Nature* **425**, 707–711.

TRIANTAFYLLOU, M.S., TRIANTAFYLLOU, G.S. & YUE, D.K.P. 2000 Hydrodynamics of fishlike swimming. *Annu. Rev. Fluid Mech.* **32**, 33–53.

UDDIN, E., HUANG, W. & SUNG, H.J. 2013 Interaction modes of multiple flexible flags in a uniform flow. *J. Fluid Mech.* **729**, 563–583.

VAN EYSDEN, C.A. & SADER, J.E. 2006 Resonant frequencies of a rectangular cantilever beam immersed in a fluid. *J. Appl. Phys.* **100** (11), 114916.

VOGEL, S. 1984 Drag and flexibility in sessile organisms. *Am. Zool.* **24** (1), 37–44.

VOGEL, S. 1989 Drag and reconfiguration of broad leaves in high winds. *J. Expl Bot.* **40** (8), 941–948.

WATANABE, Y., SUZUKI, S., SUGIHARA, M. & SUEOKA, Y. 2002 An experimental study of paper flutter. *J. Fluids Struct.* **16** (4), 529–542.

WILLIAMSON, C.H.K. & GOVARDHAN, R. 2004 Vortex-induced vibrations. *Annu. Rev. Fluid Mech.* **36** (1), 413–455.

WU, T.Y. 2011 Fish swimming and bird/insect flight. *Annu. Rev. Fluid Mech.* **43**, 25–58.

WU, X., GE, F. & HONG, Y. 2012 A review of recent studies on vortex-induced vibrations of long slender cylinders. *J. Fluids Struct.* **28**, 292–308.

ZHANG, C., HUANG, H. & LU, X.-Y. 2020 Effect of trailing-edge shape on the self-propulsive performance of heaving flexible plates. *J. Fluid Mech.* **887**, A7.

ZHANG, J., CHILDRESS, S., LIBCHABER, A. & SHELLEY, M. 2000 Flexible filaments in a flowing soap film as a model for one-dimensional flags in a two-dimensional wind. *Nature* **408**, 835–839.

ZHU, L. 2008 Scaling laws for drag of a compliant body in an incompressible viscous flow. *J. Fluid Mech.* **607**, 387–400.

ZHU, L. 2009 Interaction of two tandem deformable bodies in a viscous incompressible flow. *J. Fluid Mech.* **635**, 455–475.

ZHU, L. & PESKIN, C.S. 2002 Simulation of a flapping flexible filament in a flowing soap film by the immersed boundary method. *J. Comput. Phys.* **179** (2), 452–468.

ZHU, L. & PESKIN, C.S. 2003 Interaction of two flapping filaments in a flowing soap film. *Phys. Fluids* **15** (7), 1954–1960.